RESEARCH ARTICLE | FEBRUARY 24 2026

Helmholtz-guided suppression of spurious currents in multicomponent pseudopotential model for high-fidelity immiscible flow in porous media

Jingsen Feng ; Chuanxi Wang; Yingyang Guo ; Yang Liu ; Jingchun Min ; Moran Wang; Ke Xu

Physics of Fluids 38, 026611 (2026)
https://doi.org/10.1063/5.0313522

Physics of Fluids ARTICLE pubs.aip.org/aip/pof

Helmholtz-guided suppression of spurious currents in multicomponent pseudopotential model for high-fidelity immiscible flow in porous media

Cite as: Phys. Fluids **38**, 026611 (2026); doi: 10.1063/5.0313522
Submitted: 23 November 2025 · Accepted: 9 February 2026 ·
Published Online: 24 February 2026

Jingsen Feng,[1,2,3] Chuanxi Wang,[2] Yingyang Guo,[2] Yang Liu,[3] Jingchun Min,[3] Moran Wang,[3] and Ke Xu[2,a)]

AFFILIATIONS

[1]National Energy Shale Oil Research and Development Center, Beijing, China
[2]School of Mechanics and Engineering Science, Peking University, Beijing 100871, China
[3]Department of Engineering Mechanics, Tsinghua University, Beijing 100084, China

[a)]Author to whom correspondence should be addressed: kexu1989@pku.edu.cn

ABSTRACT

Accurately modeling immiscible fluid flow in disordered media remains a significant challenge due to the interference of spurious currents. Using the multiple-relaxation-time (MRT) multicomponent pseudopotential lattice Boltzmann method as an exemplar, we perform a Helmholtz decomposition on the anisotropic residual of discrete interaction forces to elucidate its coupling to viscosity pathways. The solenoidal component dissipates through shear viscosity (μ), while the irrotational component engages bulk viscosity (ζ), establishing distinct routes for suppressing spurious currents. Numerical experiments show that employing a 10th-order interaction force markedly reduces the solenoidal share of the residual—by three to four orders of magnitude compared to fourth-order schemes—thereby activating bulk-viscosity control via the energy-mode relaxation parameter (s_e, s_ϵ). This approach attains spurious capillary numbers as low as 10^{-5} and maintains stability at high viscosity ratios, representing up to two orders of magnitude improvement over MRT color-gradient models. The methodology is validated through Laplace pressure tests, two-component Poiseuille flow, Taylor–Bretherton bubble dynamics, and applications in digitized porous media under challenging wettability conditions and high viscosity ratios. From analysis to implementation, the present framework advances high-fidelity multiphase simulations in complex geometries at high viscosity ratios.

I. INTRODUCTION

Immiscible multiphase flow in disordered/porous media is central to subsurface energy systems, fuel cells, and microfluidics.[1–4] At the pore scale, the lattice Boltzmann method (LBM) has become a workhorse owing to its locality, geometric flexibility, and straightforward treatment of interfaces.[5,6] Mature formulations span color-gradient, pseudopotential, free-energy and phase-field variants and have been widely applied to quantify saturation-dependent transport, wettability effects, and viscous coupling.[7–9]

A persistent bottleneck, however, is the appearance of spurious currents—nonphysical velocities near curved interfaces that originate from discrete-force anisotropy and truncation errors.[10–12] Their footprint is particularly severe in low-capillary-number regimes and at high viscosity ratios, where the parasitic velocity scale can rival the physical one and corrupt mobility estimates, stability and interpretation. Recent spurious-current mitigation has increasingly focused on restoring discrete force balance, via (i) higher-order/central-moment color-gradient equilibria and recoloring operators;[13,14] (ii) isotropy-augmented and central-moment pseudopotential formulations, including robust curved-wetting treatments at large property ratios;[9,15] and (iii) well-balanced or regularized phase-field designs that recover a quiescent equilibrium at the discrete level.[16–18] Although multiple-relaxation-time (MRT)/central-moment collisions provide additional relaxation channels and improved stability in large-contrast two-phase simulations,[14,18] a predictive physical mechanism explaining when and why tuning specific relaxation parameters attenuates spurious currents is still lacking.

This work provides that missing mechanism. Starting from a two-component MRT pseudopotential model with explicit forcing, we

perform a Helmholtz–Hodge decomposition (HHD) of the residual discrete intercomponent force.[19–23] In Fourier space, the residual splits into an irrotational (longitudinal) part and a solenoidal (transverse) part,[19,24,25] which couple to the flow through distinct viscosity channels: the longitudinal response is controlled by the bulk (longitudinal) viscosity $\lambda = \zeta + \frac{4}{3}\mu$ governed by s_e, s_ϵ, whereas the transverse response is controlled solely by the shear viscosity μ governed by s_ν. Under a 10th-order isotropic construction (E10), high-order isotropy makes the residual predominantly irrotational—so tuning s_e, s_ϵ is an effective and principled lever. In contrast, low-order stencils (E4) leave a mainly solenoidal residual for which bulk-viscosity tuning has little influence.

The choice of Helmholtz–Hodge decomposition as the analytical framework is motivated by its fundamental role in separating compressive/irrotational and vortical/solenoidal content in vector fields. In Boltzmann-equation-based and LBM-coupled studies, HHD has proved particularly valuable for diagnosing artifacts and developing hybrid methods. Qi *et al.* employed HHD to separate solenoidal and compressive components in mesoscopic Boltzmann simulations of incompressible turbulence, enabling the analysis and removal of spurious pressure oscillations.[26] O'Reilly and co-workers formulated a Helmholtz-split perturbation LBM, coupling an inviscid field to a viscous perturbation field through a decomposition that has since been extended to hybrid LBM–potential-flow LES settings.[22,23] Related projection/Hodge ideas also appear in LBM-based divergence cleaning for MHD.[27] Building on these precedents, we apply HHD directly to the intercomponent-force residual and establish the mapping between the two Helmholtz channels and distinct MRT viscosity controls.

Practically, under sufficiently high-order isotropy (E10) where the residual is predominantly irrotational, the steady spurious-current amplitude follows a $1/\lambda$ scaling; decreasing s_e and s_ϵ, therefore, provides a principled and effective lever for suppression. Building on this insight, we construct a 10th-order isotropic force (E10) that eliminates lattice-tensor anisotropy up to rank 10, thereby rendering the residual overwhelmingly irrotational and activating the longitudinal damping pathway. Quantitatively, the solenoidal share of the residual drops by 3–4 orders of magnitude relative to E4, which translates into two-order-of-magnitude reductions in spurious capillary number and stable simulations at high viscosity ratios.

This work makes three principal contributions: first, we establish a model-agnostic mechanism linking the rotational character of discrete-force errors to distinct viscosity controls in MRT via Helmholtz projections, thereby unifying the conditions under which s_e, s_ϵ tuning is effective. Second, we develop an MRT pseudopotential scheme that combines E10 forcing with longitudinal-viscosity tuning (via s_e, s_ϵ) to suppress spurious currents without compromising surface-tension fidelity. Third, we provide comprehensive validation through Laplace pressure tests, two-component Poiseuille flow including viscosity-modification for large ratios, Taylor–Bretherton bubbles, and pore-scale flows in digitized media under extreme wettability and high viscosity ratios.

The practical implementation follows a clear strategy: high-order isotropy shifts the error spectrum into the irrotational channel, after which calibration of s_e, s_ϵ raises λ until the spurious capillary number falls well below the target physical capillary number. This longitudinal-control paradigm is compatible with three-dimensional extensions and graphics processing unit (GPU) implementations, providing new pathways for advancing high-precision multiphase-flow models. The remainder of this paper is organized as follows: Sec. II formalizes the MRT–NS mapping and the force decomposition, quantifies the residual's rotational content across stencils and demonstrates parameter sensitivity; Sec. III presents validations and applications; Sec. IV summarizes implications and extensions.

II. MULTICOMPONENT PSEUDOPOTENTIAL MODEL

A. MRT explicit forcing scheme

The multiple-relaxation-time (MRT) collision operator provides superior stability and accuracy compared to single-relaxation-time (SRT) schemes, particularly for multiphase flows in complex porous media.[28–30] In this section, we establish the MRT formulation and derive the key mapping between MRT relaxation parameters and macroscopic viscosities, which is essential for understanding how to control spurious currents.

1. Units and notation

Unless otherwise specified, we work in lattice units with a reference density $\rho_0 = 1$, lattice spacing $\Delta x = 1$, and time step $\Delta t = 1$, so that $c = 1$ and $c_s^2 = c^2/3 = 1/3$. If physical units are retained, keep Δt explicit and use $c_s^2 = c^2/3$ consistently.

2. Basic MRT formulation

With an external force, the discrete lattice-Boltzmann equation[29,31–33] for component σ reads

$$f^\sigma(\boldsymbol{x} + \boldsymbol{e}_i\Delta t,\, t + \Delta t) - f_i^\sigma(\boldsymbol{x}, t) = -(T^{-1}S^\sigma T)\left(\boldsymbol{f}^\sigma - \boldsymbol{f}^{\sigma(eq)}\right) + \Delta t\left(T^{-1}\left(I - \frac{S^\sigma}{2}\right)T\right)\boldsymbol{\mathcal{F}}^\sigma, \quad (1)$$

where $\boldsymbol{f}^\sigma = (f_0^\sigma, \ldots, f_8^\sigma)^\top$, $\boldsymbol{f}^{\sigma(eq)}$ are the distribution and equilibrium vectors of component σ, respectively; $\boldsymbol{e}_i$ are the discrete lattice velocities; and $\boldsymbol{\mathcal{F}}^\sigma = (\mathcal{F}_0^\sigma, \ldots, \mathcal{F}_8^\sigma)^\top$ denotes the *discrete forcing source* (Guo scheme). Here, T is the moment-transformation matrix, S^σ is the (diagonal) relaxation matrix, and I is the identity; their explicit forms are given below for D2Q9.

3. Moment basis and relaxation

The transformation matrix T maps distribution functions to moments. For D2Q9, we adopt the orthogonal d'Humières/Lallemand–Luo basis[28,29]

$$T = \begin{bmatrix} 1 & 1 & 1 & 1 & 1 & 1 & 1 & 1 & 1 \\ -4 & -1 & -1 & -1 & -1 & 2 & 2 & 2 & 2 \\ 4 & -2 & -2 & -2 & -2 & 1 & 1 & 1 & 1 \\ 0 & 1 & 0 & -1 & 0 & 1 & -1 & -1 & 1 \\ 0 & -2 & 0 & 2 & 0 & 1 & -1 & -1 & 1 \\ 0 & 0 & 1 & 0 & -1 & 1 & 1 & -1 & -1 \\ 0 & 0 & -2 & 0 & 2 & 1 & 1 & -1 & -1 \\ 0 & 1 & -1 & 1 & -1 & 0 & 0 & 0 & 0 \\ 0 & 0 & 0 & 0 & 0 & 1 & -1 & 1 & -1 \end{bmatrix}. \quad (2)$$

The diagonal relaxation matrix is

$$S^\sigma = \mathrm{diag}\left[s_\rho^\sigma, s_e^\sigma, s_\epsilon^\sigma, s_j^\sigma, s_q^\sigma, s_j^\sigma, s_q^\sigma, s_\nu^\sigma, s_\nu^\sigma\right], \quad \text{with } s_\rho^\sigma = s_j^\sigma = 1. \quad (3)$$

The relaxation rates have distinct physical meanings:[28,29] s_e^σ controls the energy/trace moment, s_ϵ^σ affects a higher-order energy moment, s_q^σ

governs heat-like fluxes, and s_ν^σ determines the shear viscosity[29,34] through

$$\nu_\sigma = c_s^2\left(\frac{1}{s_\nu^\sigma}-\frac{1}{2}\right)\Delta t = \frac{c^2}{3}\left(\frac{1}{s_\nu^\sigma}-\frac{1}{2}\right)\Delta t. \tag{4}$$

4. Equilibrium distribution and forcing

The equilibrium distribution follows a second-order Maxwellian expansion[28,29]

$$f_i^{\sigma(eq)}(\boldsymbol{x},t) = \rho_\sigma\,\omega_i\left[1+\frac{\boldsymbol{e}_i\cdot\boldsymbol{u}^{eq}}{c_s^2}+\frac{(\boldsymbol{e}_i\cdot\boldsymbol{u}^{eq})^2}{2c_s^4}-\frac{|\boldsymbol{u}^{eq}|^2}{2c_s^2}\right], \tag{5}$$

with weights $\omega_0 = 4/9$, $\omega_{1-4} = 1/9$, $\omega_{5-8} = 1/36$, lattice vectors

$$\boldsymbol{e} = \begin{bmatrix} 0 & 1 & -1 & 0 & 0 & 1 & -1 & -1 & 1 \\ 0 & 0 & 0 & 1 & -1 & 1 & 1 & -1 & -1 \end{bmatrix},$$

and the lattice sound speed c_s (defined above). The mixture equilibrium velocity is

$$\boldsymbol{u}^{eq} = \frac{\sum_\sigma \rho_\sigma \boldsymbol{u}_\sigma}{\sum_\sigma \rho_\sigma}. \tag{6}$$

Macroscopic variables[28,29] are

$$\rho_\sigma = \sum_{i=0}^{8} f_i^\sigma, \qquad \rho_\sigma \boldsymbol{u}_\sigma = \sum_{i=0}^{8} \boldsymbol{e}_i f_i^\sigma + \frac{\Delta t}{2}\boldsymbol{F}^\sigma. \tag{7}$$

We employ the Guo forcing scheme[31,32,35] for the *discrete* source

$$\mathcal{F}_i^\sigma = \omega_i\left[\frac{\boldsymbol{e}_i-\boldsymbol{u}^{eq}}{c_s^2}+\frac{(\boldsymbol{e}_i\cdot\boldsymbol{u}^{eq})\,\boldsymbol{e}_i}{c_s^4}\right]\cdot\boldsymbol{F}^\sigma, \tag{8}$$

where $\boldsymbol{F}^\sigma$ is the *macroscopic* total force acting on component σ including both fluid–fluid and fluid–solid interactions,

$$\boldsymbol{F}_f^\sigma(\boldsymbol{x}) = -g_{\sigma\sigma'}\,\psi_\sigma(\boldsymbol{x})\sum_{i=0}^{n} w(|\boldsymbol{e}_i|^2)\,\psi_{\sigma'}(\boldsymbol{x}+\boldsymbol{e}_i)\,\boldsymbol{e}_i, \tag{9}$$

$$\boldsymbol{F}_{ads}^\sigma(\boldsymbol{x}) = -g_{\sigma w}\,\psi_\sigma(\boldsymbol{x})\sum_{i=0}^{n} w(|\boldsymbol{e}_i|^2)\,\psi_w\,s(\boldsymbol{x}+\boldsymbol{e}_i)\,\boldsymbol{e}_i. \tag{10}$$

Here, σ' denotes the other fluid component ($\sigma'\neq\sigma$); $g_{\sigma\sigma'}$ and $g_{\sigma w}$ are the fluid–fluid and fluid–solid interaction strengths, respectively; $\psi_\sigma(\boldsymbol{x})$ is the pseudopotential (a scalar function of ρ_σ), ψ_w is the prescribed wall pseudopotential, and $s(\boldsymbol{x})$ is the solid indicator ($s=1$ on solid nodes and $s=0$ on fluid nodes). The weight $w(|\boldsymbol{e}_i|^2)$ depends only on the squared lattice-vector length and the chosen isotropic stencil, and n denotes the corresponding number of discrete interaction links (excluding the rest vector), with the wall pseudo-density sampled as $\psi_w^{(\sigma)} = (1+\kappa)\frac{1}{n}\sum_{i=1}^{n}\rho_\sigma(\mathbf{x}+\mathbf{e}_i)$ [supplementary material, Eq. (S2)]. We also performed an off-grid inclined-plane droplet test at 30° to verify that this fluid–solid interaction does not induce a nonphysical droplet drift in the absence of external forcing[7,36] (see the supplementary material).

5. MRT-NS mapping and viscosity control

A Chapman–Enskog expansion to $\mathcal{O}(\epsilon^2)$ yields the steady Stokes system as follows:

$$\boldsymbol{0} = -\nabla p + \mu\nabla^2\boldsymbol{u} + \left(\zeta+\frac{1}{3}\mu\right)\nabla(\nabla\cdot\boldsymbol{u}) + \boldsymbol{\mathcal{F}}, \tag{11}$$

with total body force $\boldsymbol{\mathcal{F}} = \sum_\sigma \boldsymbol{F}^\sigma$, shear viscosity $\mu = \rho\,\nu$, and bulk ("thermodynamic") viscosity ζ. In the MRT form, these read[29,34]

$$\mu = \rho\,c_s^2\left(\frac{1}{s_\nu}-\frac{1}{2}\right)\Delta t, \quad \zeta = a_e\,\rho\,c_s^2\left(\frac{1}{s_e}-\frac{1}{2}\right)\Delta t + a_\epsilon\,\rho\,c_s^2\left(\frac{1}{s_\epsilon}-\frac{1}{2}\right)\Delta t, \tag{12}$$

with $a_e = 1/3$ and $a_\epsilon = 2/9$ for the d'Humières/Lallemand–Luo D2Q9 basis. Thus, both s_e and s_ϵ contribute to ζ; in practice, they are often set equal.

6. Viscosity coupling via Helmholtz decomposition

Taking the spatial Fourier transform of (11) ($\nabla\to i\boldsymbol{k}$, $\nabla^2\to -k^2$) gives

$$\boldsymbol{0} = -i\boldsymbol{k}\,\hat{p} - \mu k^2\hat{\boldsymbol{u}} - \left(\zeta+\frac{\mu}{3}\right)\boldsymbol{k}(\boldsymbol{k}\cdot\hat{\boldsymbol{u}}) + \hat{\boldsymbol{\mathcal{F}}}. \tag{13}$$

Introduce the solenoidal and irrotational projectors

$$\boldsymbol{P}(\boldsymbol{k}) = \boldsymbol{I} - \frac{\boldsymbol{k}\boldsymbol{k}^\top}{k^2}, \qquad \boldsymbol{Q}(\boldsymbol{k}) = \frac{\boldsymbol{k}\boldsymbol{k}^\top}{k^2}, \tag{14}$$

and define the *longitudinal viscosity*

$$\lambda \equiv \zeta + \frac{4}{3}\mu. \tag{15}$$

This definition follows from the longitudinal (irrotational) projection of Eq. (11): for $\boldsymbol{u}_\parallel \parallel \boldsymbol{k}$, the shear term $\mu\nabla^2\boldsymbol{u}$ and the compressive term $\left(\zeta+\frac{1}{3}\mu\right)\nabla(\nabla\cdot\boldsymbol{u})$ contribute additively, yielding a net longitudinal damping coefficient $\left(\zeta+\frac{4}{3}\mu\right)k^2$. Applying $\boldsymbol{P}$ and $\boldsymbol{Q}$ yields

$$\hat{\boldsymbol{u}}_\perp = \boldsymbol{P}\hat{\boldsymbol{u}} = \frac{1}{\mu k^2}\boldsymbol{P}\hat{\boldsymbol{\mathcal{F}}}, \qquad \hat{\boldsymbol{u}}_\parallel = \boldsymbol{Q}\hat{\boldsymbol{u}} = \frac{1}{\lambda k^2}\boldsymbol{Q}\left(\hat{\boldsymbol{\mathcal{F}}} - i\boldsymbol{k}\hat{p}\right), \tag{16}$$

showing that the solenoidal response is controlled by μ, while the longitudinal response is controlled by λ.

7. Pseudopotential force: Gradient hierarchy plus errors

Consider the generic Shan–Chen-type force

$$\boldsymbol{\mathcal{F}}(\boldsymbol{x}) = -G\,\phi(\boldsymbol{x})\sum_i w(|\boldsymbol{e}_i|^2)\,\Phi(\boldsymbol{x}+\boldsymbol{e}_i)\,\boldsymbol{e}_i, \tag{17}$$

with $(\phi,\Phi) = (\psi_\sigma,\psi_{\sigma'})$ for fluid–fluid interaction or $(\psi_\sigma,\psi_w s)$ for fluid–solid adhesion. Taylor-expanding $\Phi(\boldsymbol{x}+\boldsymbol{e}_i)$ and contracting lattice tensors $M_{\alpha_1\ldots\alpha_p} = \sum_i w_i\,e_{i\alpha_1}\cdots e_{i\alpha_p}$ of even rank ($p=2$, $4,\ldots,10$) yields the isotropy identities as follows:

$$M_{\alpha\beta} = m_2\,\delta_{\alpha\beta}, \qquad M_{\alpha\beta\gamma\delta} = m_4\,S^{(4)}_{\alpha\beta\gamma\delta},$$
$$S^{(4)}_{\alpha\beta\gamma\delta} = \delta_{\alpha\beta}\delta_{\gamma\delta}+\delta_{\alpha\gamma}\delta_{\beta\delta}+\delta_{\alpha\delta}\delta_{\beta\gamma}, \qquad M_{\alpha_1\ldots\alpha_6} = m_6\,S^{(6)}_{\alpha_1\ldots\alpha_6}, \tag{18}$$
$$M_{\alpha_1\ldots\alpha_8} = m_8\,S^{(8)}_{\alpha_1\ldots\alpha_8}, \qquad M_{\alpha_1\ldots\alpha_{10}} = m_{10}\,S^{(10)}_{\alpha_1\ldots\alpha_{10}}.$$

For D2Q9, $m_2 = c_s^2$ and $m_4 = c_s^4$, whereas higher m_{2p} are stencil-dependent (e.g., E10 enforces isotropy through rank 10). The contracted series becomes a gradient hierarchy (purely irrotational) plus residual errors

$$\mathcal{F} = -G\phi\left[m_2\nabla\Phi + \frac{m_4}{3!}\nabla\nabla^2\Phi + \frac{m_6}{5!}\nabla\nabla^4\Phi + \frac{m_8}{7!}\nabla\nabla^6\Phi + \frac{m_{10}}{9!}\nabla\nabla^8\Phi\right] + \boldsymbol{R}_{\text{aniso}}^{(\le 10)} + \mathcal{R}^{(>10)}. \tag{19}$$

Writing $M^{(2p)} = m_{2p}\,S^{(2p)} + \Delta^{(2p)}$ gives the anisotropy leakage

$$\boldsymbol{R}_{\text{aniso}}^{(\le 10)} = -G\phi\sum_{q=0}^{4}\frac{1}{(2q+1)!}\,\Delta^{(2q+2)} : \nabla^{2q+1}\Phi. \tag{20}$$

Helmholtz splitting of the total error $\boldsymbol{R}_{\text{total}} = \boldsymbol{R}_{\text{aniso}}^{(\le 10)} + \mathcal{R}^{(>10)}$ reveals two distinct control pathways: solenoidal errors ($\boldsymbol{P}\boldsymbol{R}_{\text{total}}$) are damped by μ and largely insensitive to s_e, s_ϵ; irrotational errors ($\boldsymbol{Q}\boldsymbol{R}_{\text{total}}$) are damped by $\lambda = \zeta + \frac{4}{3}\mu$ and, therefore, tunable via s_e, s_ϵ. This immediately explains the different parameter sensitivities of two popular stencils. **E10** enforces isotropy up to rank 10, eliminating $\Delta^{(2p)}$ for $p \le 5$.[10,37] What remains is dominated by higher-order truncation that is predominantly irrotational, making spurious currents highly responsive to longitudinal-viscosity tuning via s_e and s_ϵ.[38,39] In contrast, **E4** leaves significant low-order anisotropy ($\Delta^{(6)}, \Delta^{(8)}, \Delta^{(10)} \neq 0$), whose Helmholtz content is largely solenoidal; here spurious currents scale with the shear-viscosity channel and are, therefore, insensitive to s_e adjustments. This analysis directly translates into practical guidance for tuning the collision operator to suppress these artifacts. Specifically: (i) Use s_ν to suppress solenoidal contamination [as shown in Fig. S2(a)]; (ii) use s_e and s_ϵ together to raise ζ when the error is irrotationally dominated (typical of E10-like stencils), recalling both contribute with weights 1/3 and 2/9 in (12); and (iii) in all cases, the relevant damping for longitudinal response is $\lambda = \zeta + \frac{4}{3}\mu$.

8. Numerical validation through Fourier analysis

We validate the theoretical predictions through direct Fourier-space analysis of discrete force operators for E4 through E10 stencils.[29,32,35] This numerical verification quantifies how isotropy order affects both error magnitude and rotational character.

We construct the stencil weights by enforcing isotropy constraints up to order $2K$ (where $K = 2, 3, 4, 5$ for E4, E6, E8, and E10, respectively) through a least squares solution of the moment equations. For each stencil, we compute the Fourier symbol $\hat{\boldsymbol{F}}(\boldsymbol{k})$ of the discrete force operator and decompose it into components parallel and perpendicular to the wavevector $\boldsymbol{k}$. The parallel component $|\hat{F}_\parallel|$ represents irrotational (gradient-like) contributions that can be expressed as pressure gradients, while the perpendicular component $|\hat{F}_\perp|$ captures solenoidal (vortex-like) errors that cannot be absorbed into a pressure tensor.

The following figures present three key metrics across the physically meaningful wavenumber range $0 < k < \pi$ (beyond which aliasing occurs on the discrete lattice). Figure 1(a) shows the relative error amplitude $|\boldsymbol{F}_{\text{err}}|/|\boldsymbol{F}_{\text{iso}}|$, where the error is defined as the deviation from the ideal isotropic linear response. As expected, E4 exhibits the largest errors, while E10 maintains minor errors across the entire spectrum. This order-of-magnitude improvement directly translates to reduced spurious currents in practical simulations.

More revealing is the decomposition shown in Figs. 1(b) and 1(c). Figure 1(b) displays the solenoidal fraction within the error component alone, $|\boldsymbol{F}_\perp|/|\boldsymbol{F}_{\text{err}}|$. For E4, this ratio approaches unity at moderate wavenumbers, indicating that the errors are predominantly solenoidal and, thus, cannot be controlled through bulk viscosity adjustments. In stark contrast, E10 maintains a much lower solenoidal fraction, with most of its (already small) error being irrotational. Figure 1(c) shows the solenoidal share in the total driving force, confirming that higher-order stencils progressively reduce the vortex-generating components that are most difficult to suppress.

The Fourier analysis confirms our theoretical framework: E10 achieves superior spurious current suppression through (i) order-of-magnitude reduction in total error compared to E4 and (ii) predominantly irrotational error structure amenable to bulk viscosity control.[10,37–39] Conversely, E4's large solenoidal errors remain unaffected by s_e tuning, necessitating different optimization strategies. These findings establish high-order isotropy as essential for applications demanding low spurious currents with high viscosity ratios.

9. Simulation-based Fourier/Helmholtz validation

To directly corroborate the mechanism in full simulations, we perform a Helmholtz–Hodge decomposition in Fourier space on the *simulated* intercomponent force fields. For each stencil (E4/E6/E8/E10), we

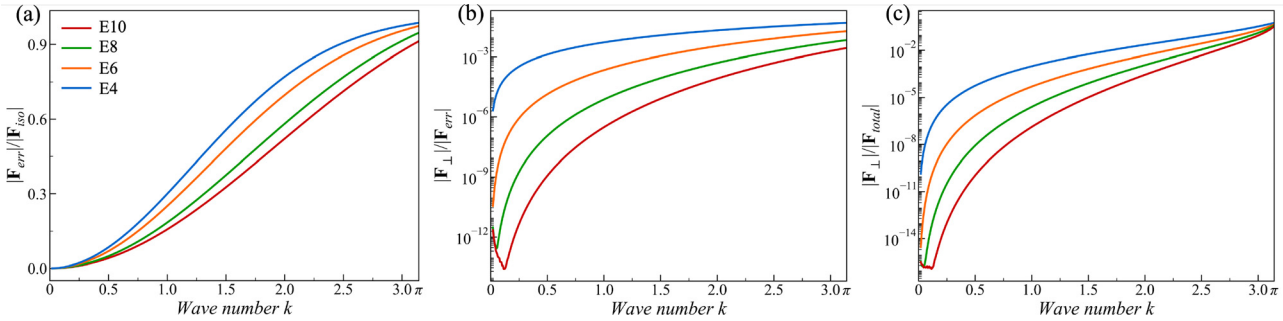

FIG. 1. Fourier-space analysis of discrete force operators for E4 through E10 stencils. (a) Relative error amplitude compared to the isotropic reference, showing order-of-magnitude reduction from E4 to E10. (b) Solenoidal (rotational) fraction within the error component, revealing that E4 errors are predominantly vortex-like while E10 errors are mostly gradient-like. (c) Solenoidal fraction in the total force, demonstrating systematic improvement with the stencil order. The wavenumber range extends to $k = \pi$, the Nyquist limit for discrete lattices. Color scheme: E4 (blue), E6 (orange), E8 (green), and E10 (red).

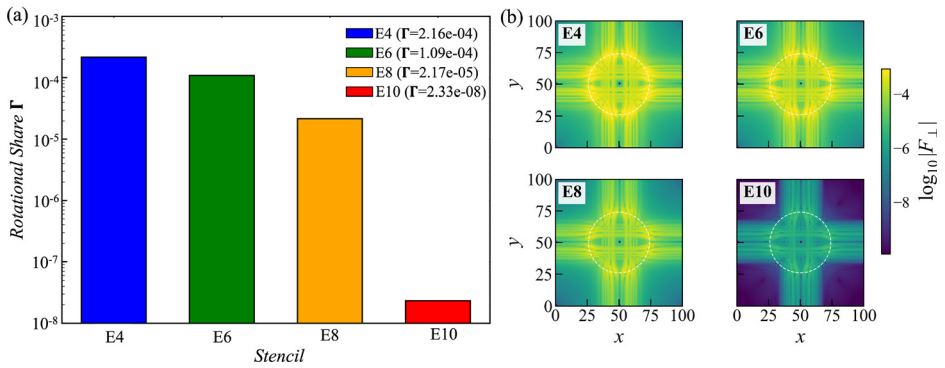

FIG. 2. Simulation-based Fourier/Helmholtz validation. (a) Global L2 rotational share Γ computed from the simulated force fields shows a monotonic reduction from E4 to E10, with E10 orders of magnitude lower than E4. (b) Spatial map of $\log_{10}|\boldsymbol{F}_\perp|$ for the four stencils (same color scale), where stripe-like vortex artifacts are visibly suppressed when increasing the isotropy order. Both diagnostics independently confirm that high-order isotropy converts the residual forcing into a predominantly irrotational signal that is amenable to bulk-viscosity control.

take the steady force field from a periodic droplet test, compute the discrete Fourier transform, and project onto longitudinal and transverse subspaces using $\boldsymbol{P}$ and $\boldsymbol{Q}$, respectively. Two complementary diagnostics are reported: (i) the global L2 rotational share $\Gamma = ||\boldsymbol{F}_\perp||_2^2/(||\boldsymbol{F}_\perp||_2^2 + ||\boldsymbol{F}_\parallel||_2^2)$ and (ii) the spatial distribution of the rotational magnitude $\log_{10}|\boldsymbol{F}_\perp|$, shown in Fig. 2. The left panel shows that increasing the isotropy order systematically reduces the rotational share, confirming that the residual forcing is progressively shifted from the transverse (solenoidal) channel toward the longitudinal (irrotational) channel that can be damped by λ. The right panel further visualizes how the transverse forcing becomes more localized and much weaker for E8/E10, with the stripe-like vortex artifacts strongly suppressed, consistent with the observed reductions in spurious currents in physical-space tests.

10. Rationale for comparisons with color-gradient models

The foregoing MRT–NS mapping and Helmholtz analysis provide a direct theoretical basis for the numerical benchmarks reported next (Sec. II B). In these tests, we contrast the behavior of the E4 pseudopotential stencil against a modern MRT color-gradient formulation. This comparison is strictly motivated by the widespread adoption of color-gradient methods in pore-scale two-phase studies and relative-permeability assessments for porous media.[2,5,40–50] Details of the MRT color-gradient model used here are summarized in the supplementary material. By establishing the color-gradient model as a representative baseline, we aim to contextualize the performance of the proposed high-order spectral suppression technique in complex geometries.

11. Model-agnostic diagnostics vs model-specific control

While the specific suppression mechanism explored here—tuning energy-mode relaxation rates to damp longitudinal errors—is framed around multicomponent pseudopotential models, the underlying Helmholtz–Hodge decomposition is model-agnostic. For any multiphase LBM formulation, whether pseudopotential, free-energy, or color-gradient, the parasitic velocity field (or its driving force) can be decomposed into solenoidal and irrotational parts. This provides a universal diagnostic for determining whether spurious motion is predominantly vortical or compressive.

However, the effective control lever depends strictly on the spectral signature of the model. In pseudopotential formulations, numerical imbalance in the explicit interaction force often creates a nontrivial irrotational contribution (nonzero discrete divergence). This directly excites the longitudinal mode, which in MRT-LBM is efficiently damped by the bulk viscosity via the relaxation rates s_e and s_ϵ. Conversely, in color-gradient models, capillarity is realized through a perturbation operator followed by a recoloring step. As noted in the theoretical analysis, this sequence typically generates a residual that is predominantly solenoidal. Consequently, the spurious currents couple to the shear viscosity (μ) rather than the bulk viscosity, rendering s_e and s_ϵ ineffective as control parameters. This dichotomy explains why parameter strategies successful for high-order pseudopotential schemes (E10) do not transfer to color-gradient or low-order (E4) schemes. The decomposition, thus, serves not only to validate the proposed bulk-viscosity damping for E10 but also to clarify the limiting factors in alternative formulations. With this context, the forthcoming figures use the color-gradient model as a practically relevant baseline to benchmark spurious currents, while the E10 results illustrate how shifting the residual toward the longitudinal channel enables effective bulk-viscous control.

B. Reduction of spurious currents

Proper selection of relaxation times plays a pivotal role in suppressing spurious currents. As clarified above, the steady amplitude depends on the *longitudinal* viscosity $\lambda = \zeta + \frac{4}{3}\mu$ for irrotational residuals and on the *shear* viscosity μ for solenoidal residuals. In D2Q9 MRT, the bulk/longitudinal viscosity receives contributions from both the energy moment e (via s_e with coefficient $1/3$) and the ϵ-moment (via s_ϵ with coefficient $2/9$). Therefore, reducing s_e and s_ϵ together effectively increases ζ and decreases the spurious-current level when a high-order (E10) intercomponent forcing is used.

For the two components, we adopt the same s_e^σ and s_ϵ^σ, and thus, in what follows, we drop the superscript and denote them simply by s_e and s_ϵ. Two representative cases are examined to demonstrate how these parameters impact the suppression of spurious currents.

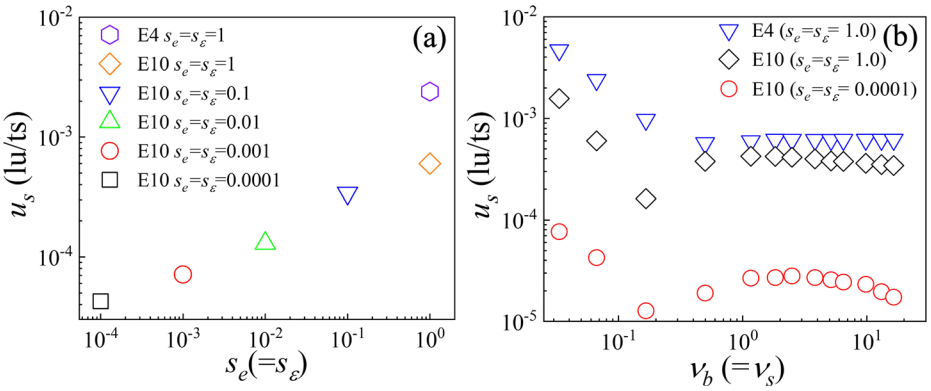

FIG. 3. (a) Maximum spurious currents of E4 and E10 models under varying s_e and s_ϵ with $\upsilon_b = \upsilon_s = 0.0667$. (b) Variation of the maximum spurious currents with kinematic viscosity.

1. Static bubble

The first one is a static bubble with a radius of $R = 16$ embedded in the suspending fluid; the simulation domain is the same as Fig. S1(a). The fundamental principle of numerical parameters is that they do not affect the results of numerical simulations. As shown in Fig. S4, the surface tension shows good consistency under different s_e and s_ϵ.

Figure 3(a) shows maximum spurious currents of 2.4×10^{-3} (4th-order isotropy, E4) vs 4.25×10^{-5} (10th-order, E10, $s_e = s_\epsilon = 0.0001$). Figure 3(b) reveals decreasing spurious currents with increasing kinematic viscosity until stabilization. The E10 model reduces maximum spurious currents by two orders of magnitude compared to E4, E4 exhibits 6.17×10^{-4} while E10 with $s_e = s_\epsilon = 0.0001$ achieves 1.73×10^{-5}.

2. Porous media

To support porous media applications, testing complex geometry is necessary to address structural anisotropy. Here, we will illustrate that the presence of spurious currents is an inherent defect of the LB model rather than a numerical error by observing the relationship between the spurious capillary number and the increasing grid numbers. Ca_s quantifies the ratio of viscous forces caused by spurious current to interfacial tension in multiphase flow systems. A structure consisting of 64 regularly packed circles [see Fig. S5(a) in the supplementary material] are employed to assess Ca_s of the model within porous media. The number of grids describing the structure progresses from $100 \times 100\text{lu}^2$ (10 000 grids) to $1000 \times 1000\text{lu}^2$ (1 000 000 grids). We apply E10 model with $s_e = s_\epsilon = 1$ to get Ca_s and the two-phase distributions are initially preset by the random scattering method at a saturation $S_1 = S_2 = 0.5$, with kinetic viscosity $\upsilon_1 = \upsilon_2 = 0.1667$ and contact angle $\theta_1 = 85°$. As shown in Fig. S5(b), notwithstanding 100 times increase in grid numbers, Ca_s merely have a less 28% reduction magnitude, which decreases from 1.11×10^{-4} to 8×10^{-5}. This reduction can be contributed to higher resolution of the description of the porous structure with grid numbers increasing.

Then we choose the same porous media with $500 \times 500\text{lu}^2$ to compare Ca_s among E4 model, state-of-the-art MRT color-gradient model and E10 model with different parameters. All cases are under the same condition with saturation $S_1 = S_2 = 0.5$, kinematic viscosity $\upsilon_1 = \upsilon_2 = 0.0667$, contact angle $\theta_1 = 85°$, and surface tension $\gamma = 0.1543$. As shown in Fig. 4(a), the E4 model exhibits the largest Ca_s of 9.5×10^{-4}. Ca_s of the color gradient model is 3.2×10^{-4}. For E10 model, Ca_s is 7.4×10^{-5} for $s_e = s_\epsilon = 1$ while Ca_s is only 4.54×10^{-6} for $s_e = s_\epsilon = 0.0001$. Figure 4(b) shows the E10 model with $s_e = s_\epsilon = 0.0001$, which exhibits superior performance in reducing Ca_s under conditions of extreme wettability. The values are both 3.1×10^{-6} with $\theta_1 = 0$ and $\theta_1 = 180°$. In conclusion, Ca_s of E10 model reduced by two orders of magnitude compared to E4 model.

Figure 5 compares the spurious-current fields of the color-gradient model and the E10 model with $s_e = s_\epsilon = 0.0001$ at $\theta_1 = 85°$ and $\theta_1 = 180°$. The color-gradient model exhibits interface spurious currents up to 2.2×10^{-2}, while the E10 model with $s_e = s_\epsilon = 0.0001$ reduces spurious currents to 1.5×10^{-4}.

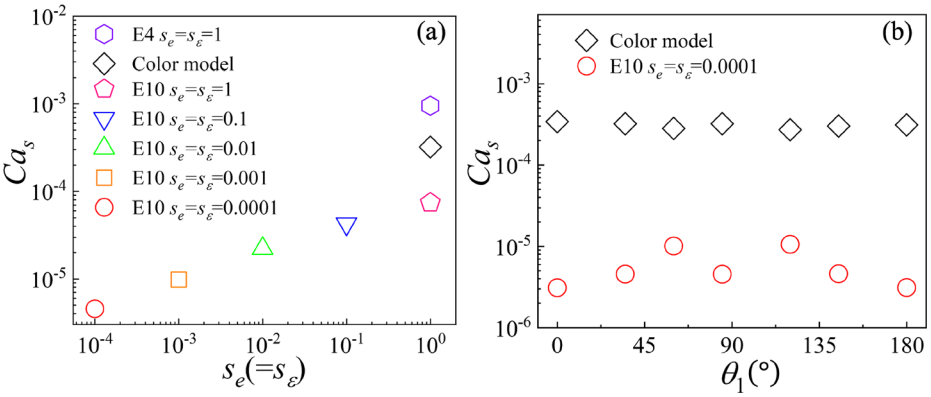

FIG. 4. (a) Spurious capillary number Ca_s for E4, state-of-the-art MRT color-gradient, and E10 models under varying s_e and s_ϵ. (b) Variation of Ca_s with contact angle for the color-gradient model and the E10 model with $s_e = s_\epsilon = 0.0001$.

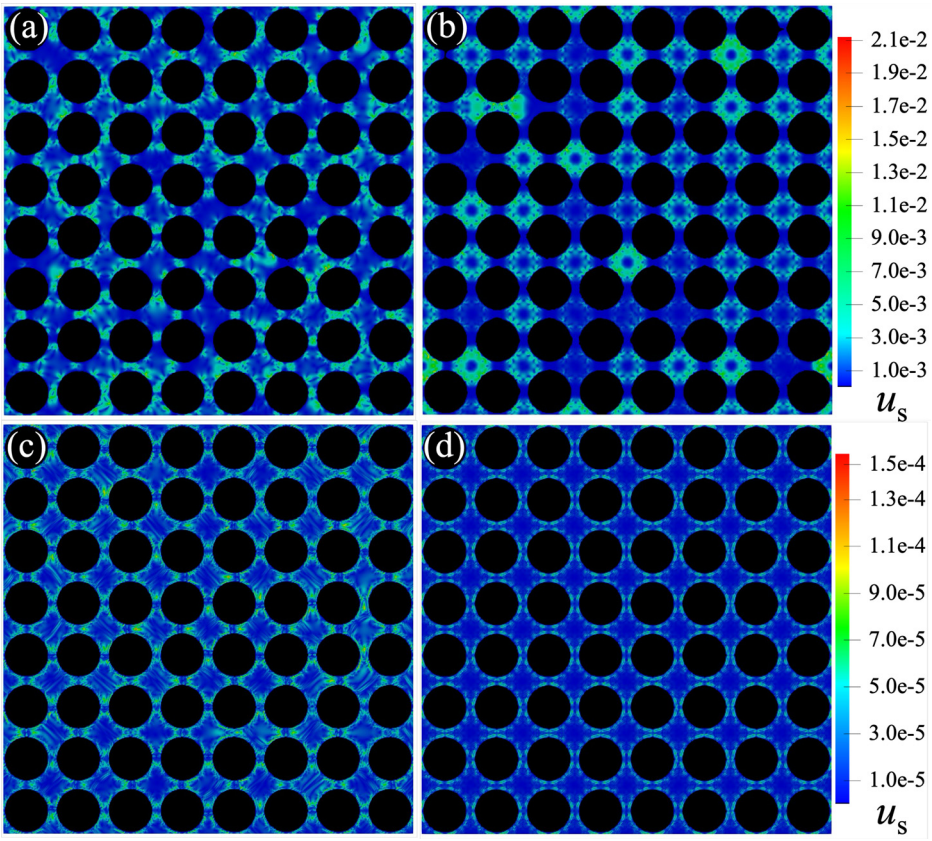

FIG. 5. Spurious-current fields in porous media. Panels (a) and (b) show the color-gradient model with $\theta_1 = 85^\circ$ and $\theta_1 = 180^\circ$, respectively; panels (c) and (d) depict the E10 model with $s_\theta = s_\epsilon = 0.0001$ at the same contact angles.

C. High viscosity ratio modification

The capability of the model in describing momentum exchange through the interface can be justified by two-component Poiseuille flow verification. In an infinite 2D horizontal channel, wetting phase flows along the channel wall and non-wetting phase flows between the wetting phase.[33,43,51–54] The thin wetting phase near the channel wall acts as a lubricant for the viscous non-wetting phase, resulting in its relative permeability far exceeding 1. The relative permeabilities of the wetting phase (K_w) and non-wetting (K_{nw}) phase can be calculated by

$$K_w = \frac{1}{2}S_w^2(3 - S_w), \tag{21}$$

$$K_{nw} = (1 - S_w)\left[\frac{3}{2}M + (1 - S_w)^2\left(1 - \frac{3}{2}M\right)\right]. \tag{22}$$

As we mentioned in Sec. II B 2, the viscosity of the low-viscosity phase must not be too small in systems with high viscosity ratios to control spurious currents and ensure numerical stability while maintaining a low spurious Reynolds number. Simultaneously, to preserve isotropy and minimize the spurious capillary number, the viscosity of the high-viscosity phase must not be too large. Considering these factors, a viscosity range of $0.0667 - 0.1667$ for the low-viscosity phase is deemed appropriate. The literature[33,55,56] shows their multicomponent pseudopotential models achieve a high viscosity ratio in two-component Poiseuille flow, as shown in Table I, but the minimum viscosity of their models is extremely small. In our model, the minimum viscosity is set as 0.0667, which is consistent with the Laplace verification in Sec. II B 1.

To achieve a relatively high viscosity ratio, our maximum viscosity is 1–2 orders of magnitude higher than that of other models. When the viscosity ratio of the components is less than 10, the numerical error caused by mixing is acceptable.[57] However, under such high viscosity and viscosity ratio conditions, the impact of a small amount of high viscosity component on the overall velocity in low viscosity

TABLE I. Viscosity parameters adopted in prior multicomponent lattice Boltzmann models and in the present work.

Quantity	Porter *et al.*[33]	Gharibi and Ashrafizaadeh[55]	Otomo *et al.*[56]	Present model
Minimum viscosity	0.000 33	0.000 167	0.0017	0.0667
Maximum viscosity	1.5	0.835	1.7	66.667
Viscosity ratio	1000	5000	1000	1000

components can lead to significant distortion in the numerical solutions. In multicomponent LBM, spontaneous diffusion leads to minor "mixing" between components,[33,55,56,58–60] which implies one grid point will possess two components at the same time, i.e.,: $\rho_1 = 1.01$ with $\rho_2 = 0.03$. We discovered that employing the color gradient model[5,43,61–63] to handle diffusion mixing can effectively resolve this issue. Interface judgment function is defined as

$$\phi(x) = \frac{\rho_1(x) - \rho_2(x)}{\rho_1(x) + \rho_2(x)}. \tag{23}$$

It is also considered that the viscosity of the mixed component diffusing into the main component at the interface is equal to the viscosity of the main component (relaxation time) to address the aforementioned numerical distortion. Interpolation is used to ensure a smooth transition of the relaxation time at the interface of the two phases as follows:

$$\tau(x) = \begin{cases} \tau_1, & \phi > \delta, \\ g_1(\phi), & \delta \geq \phi > 0, \\ g_2(\phi), & 0 \geq \phi > -\delta, \\ \tau_2, & \phi < -\delta, \end{cases} \tag{24}$$

where τ_1 and τ_2 are the relaxation times of the two components, $g_1(\phi) = s_1 + s_2\phi + s_3\phi^2$, $g_2(\phi) = t_1 + t_2\phi + t_3\phi^2$, $s_1 = t_1 = 2\tau_1\tau_2/(\tau_1 + \tau_2)$, $s_2 = 2(\tau_1 - s_1)/\delta$, $s_3 = -s_2/2\delta$, $t_2 = 2(t_1 - \tau_2)/\delta$, $t_3 = t_2/2\delta$, and $\delta = 0.8$.

From Fig. 6, the relative permeabilities of the two-component Poiseuille flow for thin wetting phase and viscous non-wetting phase obtained by our modified model align with analytical solutions, indicating that the model describes the momentum exchange correctly. Across $M = 10$–1000, the projected-viscosity treatment closely follows the analytical curves, whereas arithmetic viscosity blending exhibits a systematic underprediction of K_{nw} that becomes more pronounced as M increases. This figure, therefore, provides direct evidence that the interface-aware viscosity projection removes the mobility bias induced by diffusion mixing while preserving a smooth relaxation-time transition. By contrast, Porter's model significantly deviates from the analytical solution. To rationalize this difference, recall that two–component Poiseuille flow with zero interfacial curvature admits a shear-stress balance $\mathrm{d}\tau/\mathrm{d}y = \rho F_b$ and a local gradient $u'(y) = \tau(y)/\mu(y)$. The volumetric rate is, therefore, a weighted functional of the mobility

$$Q \propto \int_{-H}^{H} w(y)\,\mu(y)^{-1}\,\mathrm{d}y, \qquad w(y) = H - |y|. \tag{25}$$

If viscosity is blended arithmetically in a diffuse layer, $\mu_{\mathrm{mix}}(y) = \alpha(y)\mu_{\mathrm{high}} + [1 - \alpha(y)]\mu_{\mathrm{low}}$ with $\alpha \in (0, 1)$, Jensen's inequality for the convex map $f(x) = 1/x$ gives $\mu_{\mathrm{mix}}^{-1} \leq \alpha/\mu_{\mathrm{high}} + (1 - \alpha)/\mu_{\mathrm{low}}$, and hence $Q_{\mathrm{mix}} < Q_\sharp$. In other words, global mixing reduces the effective mobility and underpredicts the non-wetting relative permeability K_{nw} in (21) and (22). The bias scales with both the mixing extent (nominal interface width δ) and the absolute viscosity gap, so maintaining the same ratio M but raising the absolute viscosities amplifies the error. This explains why models operated at very small absolute viscosities and very thin interfaces accurately reproduce (21) and (22), whereas the same arithmetic blending deviates in our setting where a larger minimum viscosity is required for stability and isotropy.

Our modification avoids this bias by projecting the viscosity onto the dominant component using the color function (23) and (24), yielding a near sharp-interface viscosity field [mixing error $O(\delta)$] with a

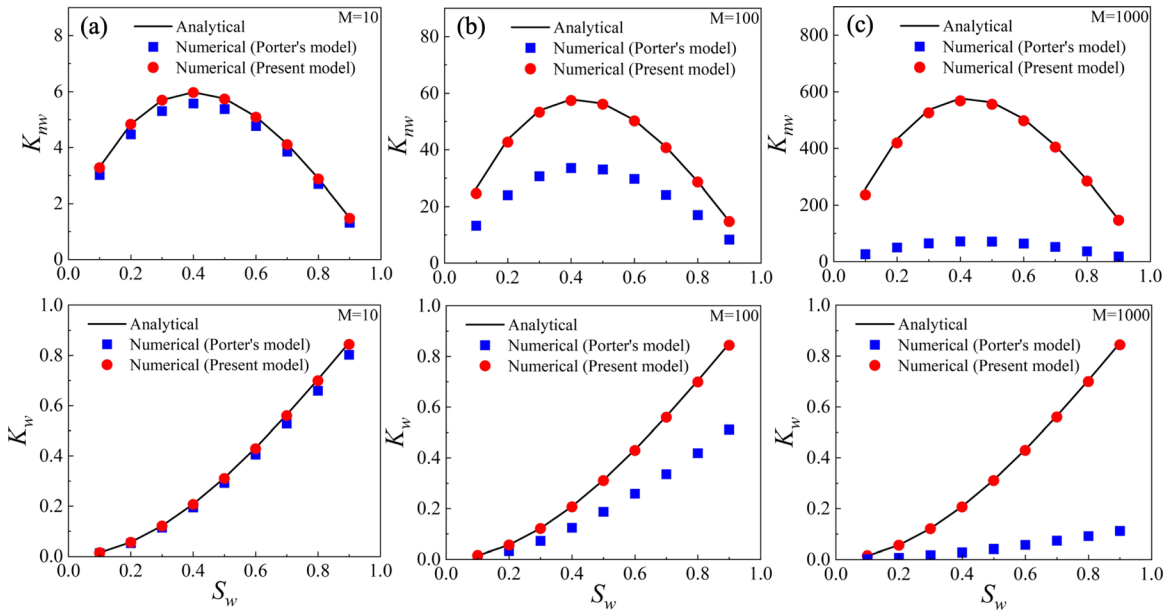

FIG. 6. Two-component Poiseuille flow for (a) $M = 10$, (b) $M = 100$, and (c) $M = 1000$. Arithmetic viscosity blending across a diffuse interface lowers the effective mobility, $Q \propto \int w(y)\,\mu^{-1}(y)\,\mathrm{d}y$, leading to an underprediction of the non-wetting relative permeability K_{nw}. Projecting viscosity via the color function (23) and (24) restores a near sharp-interface field and recovers the analytical relations.

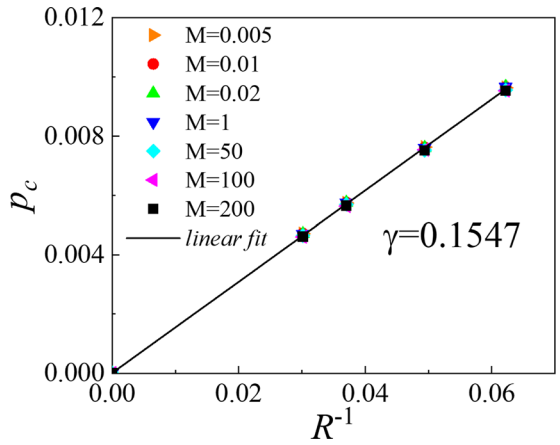

FIG. 7. Laplace verification under different viscosity ratios.

controlled, smooth transition. As a result, the analytical relations are recovered in Fig. 9 while keeping parameter choices consistent with the rest of the study.

Figure 7 shows that our model can satisfy a consistent Laplace verification under different viscosity ratios with the minimum viscosity of 0.0667, and the surface tension is the same as that in Fig. S4. The pressure jump exhibits the expected Laplace-law behavior and remains essentially unchanged as the viscosity ratio varies, demonstrating that the interfacial curvature is captured consistently. The agreement up to $M = 200$ supports the robustness of our isotropic forcing and parameter-consistent setup in the high-contrast regime relevant to the subsequent applications.

There are two points need to be clarified: (1) It can be seen in (21) and (22) that in two-component Poiseuille flow with a zero-curvature interface, surface tension serves only as a phase separation parameter with no impact on numerical results, provided sufficient phase separation is ensured. In Laplace verification, the model needs to capture nonzero curvature at the interface to realize the functionality of surface tension, so implementing Laplace verification for large viscosity ratios places a higher demand on isotropy than does two-component Poiseuille flow at large viscosity ratios. (2) To ensure the application of the model in practical physical problems, the selection of fluid viscosity for two-component Poiseuille flow and Laplace verification must be consistent as we have done. However, the literatures[33,55,56] lack consideration of parameter consistency. According to the Laplace verification in Fig. 7, the maximum viscosity ratio of the model that is applicable to all practical physical problems is 200, which is enough for most physical investigations. Our previous investigation of viscous coupling effects in porous media[60] provides an example for the application of the model.

From Fig. 8, the E10 model demonstrates superior suppression of spurious currents across viscosity ratios, especially with $s_e = s_\epsilon = 0.0001$. As introduced, model anisotropy intensifies with rising viscosity ratios. Figure 8(a) reveals consistent trends between maximum spurious currents and viscosity dependencies [Fig. 3(b)]: E4 reaches 1.3×10^{-3} at $M = 200$, while E10 with $s_e = s_\epsilon = 0.0001$ maintains 4.4×10^{-5}. In Fig. 6(b), though the spurious currents do not increase in response to the viscosity ratio, Ca_s linearly escalates with fluid viscosity for both models. Even at $M = 200$, Ca_s of the E10 model with $s_e = s_\epsilon = 0.0001$ is merely 1.01×10^{-5}, representing a 35-fold reduction in comparison to the E4 model.

The existence of porous media further increases model anisotropy and elevates spurious currents. Combining Fig. 8(b) with Fig. S6(a) shows that Ca_s in porous media exceeds that in a suspending bubble by more than an order of magnitude, imposing tighter constraints on immiscible-flow simulations. We compare Ca_s of different models within the same porous medium as Sec. II B 2. As shown in Fig. 9(a), the spurious capillary number of the E10 model with $s_e = s_\epsilon = 0.0001$ at $M = 50$ and $M = 200$ is reduced by roughly 20-fold relative to the color-gradient model under a low-viscosity-phase contact angle $\theta_1 = 85°$. Figure 9(b) further indicates that Ca_s remains remarkably small under extreme wettability ($M = 100$), taking values of 4.17×10^{-5} at $\theta_1 = 0°$ and 9.47×10^{-5} at $\theta_1 = 180°$, in contrast to 6.23×10^{-3} and 3.1×10^{-3} for the color-gradient model. These correspond to reductions of about two orders of magnitude. Figure 5(b) and Fig. S6(b) together highlight the strong performance of our model for extreme porous-media conditions.

Figure S6 illustrates that our model is capable of describing the phase behavior induced by capillary pressure under high viscosity ratios and extreme wettability within porous media. The bubble morphology remains consistent whether the bubbles represent the viscous phase or the low-viscosity phase.

Figure S7 shows that the maximum spurious currents are, respectively, 1.34×10^{-4} and 6.35×10^{-5} when bubbles act as viscous phase and low-viscosity phase. Spurious currents of the color-gradient model

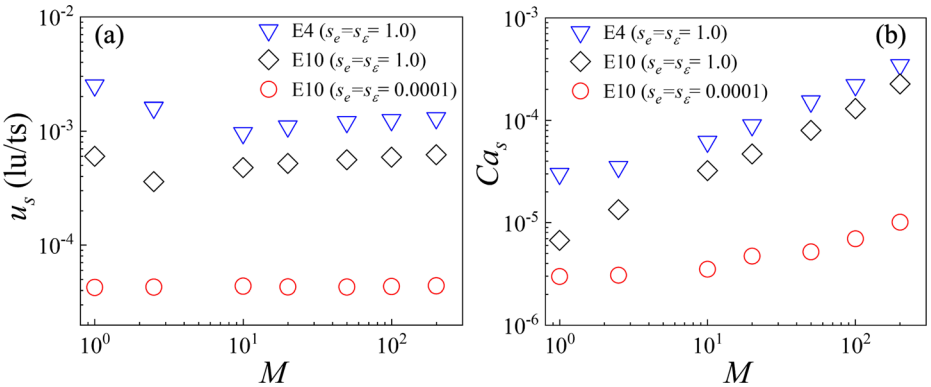

FIG. 8. Maximum spurious currents (a) and spurious capillary number (b) of a suspending bubble with $R = 16$ under different viscosity ratios.

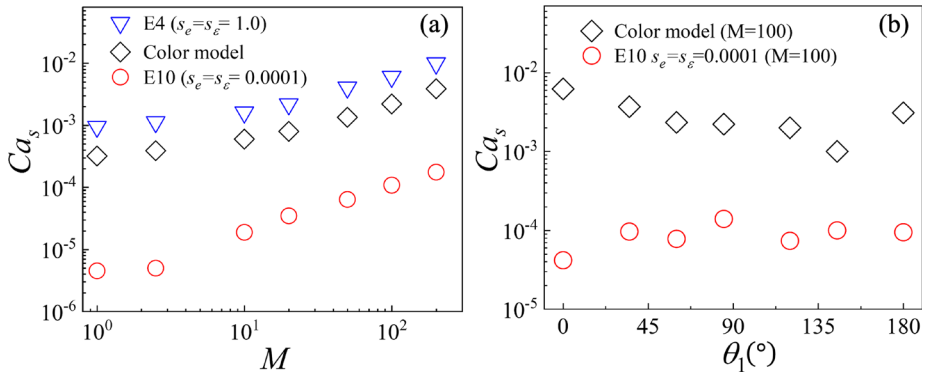

FIG. 9. (a) Spurious capillary number Ca_s for E4, state-of-the-art MRT color-gradient, and E10 models with $s_e = s_\epsilon = 0.0001$ under different viscosity ratios. (b) Variation of Ca_s with contact angle for the color-gradient model and the E10 model with $s_e = s_\epsilon = 0.0001$.

are 1.42×10^{-2} and 1.1×10^{-2}, which are over two orders of magnitude larger than those of E10 model with $s_e = s_\epsilon = 0.0001$.

III. APPLICATIONS

A. Taylor/Bretherton flow

We conduct a series of simulations for the Taylor/Bretherton flow with Ca_s significantly smaller than the prescribed value. The Taylor/Bretherton flow[64–69] describes the motion of a long gas bubble through a liquid (water here) in a narrow channel, as illustrated in Fig. S8. It has been observed that the thickness of the water film has relationship with $Ca^{2/3}$. The capillary number is defined as[66]

$$Ca = \frac{\mu_{\text{water}} U_{\text{bubble}}}{\gamma}, \tag{26}$$

where μ_{water} is the water viscosity, U_{bubble} is the bubble velocity, and γ is the surface tension between water and bubble interface.

Bretherton investigated the motion of a long bubble in a liquid-filled tube and found the film thickness δ proportional to $Ca^{2/3}$ when Ca is small. Subsequently, Taylor refined and extended Bretherton's law to a broader range of capillary numbers through extensive experiments as[64,65]

$$\frac{\delta}{H} = 1.34Ca^{2/3}/(1 + 1.34^{*}2.5Ca^{2/3}), \tag{27}$$

where H is the height of the capillary tube; the coefficient 1.34 is derived by Bretherton, and the coefficient 2.5 is empirical.

Inertia can be neglected here. The spurious capillary number in this system is 0.000 33. The densities of water and bubble are uniform 1, while the actual density ratio in the experiments is much larger than 1. In addition, the maximum Reynolds number in our simulations is 7.2. Giavedoni and Saita[68] found that Reynolds number effects are negligible for $Ca \leq 0.05$ and have a moderate impact for $Ca > 0.05$, within a Reynolds number range of 0–70. Furthermore, Heil[69] extended the analysis to Re up to 300, showing that the Reynolds number has a limited impact on the established film thickness, with only a 7% variation compared to the $Re = 0$ case. Accordingly, we can disregard inertia effects and conclude that the primary governing parameter for microchannel Bretherton flows is viscosity ratio.

Figure 10 shows that our model captures the liquid film in Taylor/Bretherton flow with low Ca. The simulated liquid-film thicknesses agree well with Taylor's empirical equation. The simulation range of Ca is set to 0.002–1. The water and bubble kinematic viscosities are 16.667 and 0.1667 in all cases, respectively, so the viscosity ratio $M = \rho_w\nu_w/\rho_b\nu_b = 100$, which matches the physical properties. The surface tension is $\gamma = 0.1543$. To save computational resources, high-resolution grids are only used for the low-Ca cases, i.e., 1600×402 for $Ca = 0.002$, 800×202 for $Ca = 0.005$, 0.01, and 0.02, 600×152 for $Ca = 0.05$ and 0.1, and 400×102 for $Ca = 0.2$, 0.5, and 1, with the bubble width exceeding 2/3 of the channel height.[67] Moreover, the relaxation parameters s_e and s_ϵ differ for different Ca. We choose $s_e = s_\epsilon = 0.0001$ for $Ca = 0.002$, $s_e = s_\epsilon = 0.0005$ for $Ca = 0.005$, 0.01, and 0.02, $s_e = s_\epsilon = 0.005$ for $Ca = 0.05$ and 0.1, and $s_e = s_\epsilon = 0.01$ for $Ca = 0.2$, 0.5, and 1 to ensure that Ca remains sufficiently

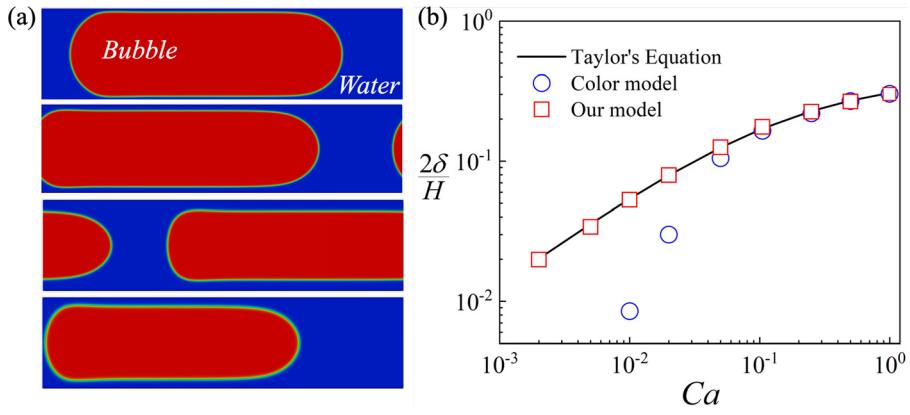

FIG. 10. (a) Bubble shapes computed for $Ca = 0.005$, 0.02, 0.1, and 0.5 (top to bottom). (b) Liquid-film thickness vs capillary number.

small. Higher relaxation parameters can then be adopted to accelerate convergence once the *Ca* effect is controlled. Spurious currents interfere with the accurate computation of viscous forces. As illustrated in Fig. 10(b), the color-gradient model fails to characterize liquid-film thickness at low capillary numbers. Upon further reduction of *Ca*, spurious capillary numbers overwhelm the physical response, leading to the disappearance of shear effects and the elimination of the liquid film.

B. Startup of trapped ganglia in porous media

Nonwetting ganglia can become trapped by capillary forces at the pore-throat, a phenomenon known as capillary trapping.[70,71] The capillary trapping of ganglia alters the flow channels,[72,73] thereby significantly influencing flow dynamics, mass and heat transport, and chemical reactions[1,74,75] within the medium. To mobilize a trapped ganglion in porous media, an external driving force exceeding a certain threshold is required to overcome the capillary pressure barrier.[76–79] Wang and Xu[80] investigated the initiation process of an initially trapped ganglion in porous media. Through a theoretical analysis conducted in a 2D conceptual model of porous media, they developed a theory for the startup criteria. The media consists of a rectangular array of identical circular grains, as shown in Fig. S9.

They introduced a modified Bond number as

$$B_o = \frac{2|\nabla P|R_0}{\gamma/R_0} = \frac{2|\nabla P|R_0^2}{\gamma}, \tag{28}$$

where ∇P denotes the external pressure gradient, so $2|\nabla P|R_0$ is the pressure drop over a pore length. $2\gamma/R_0$ is the reference capillary pressure. According to their theory, a bubble volume is nV_{pore} which initially occupies n pores has a critical start up Bond number Bo_c. The values of Bo_c for $n = 7, 8, 9, 10, 11$ are 0.138, 0.123, 0.101, 0.098, and 0.086, respectively. We follow the same set up with $R_0 = 60$ and $\gamma = 0.1543$; the simulated Bo_c align well with theoretical values in Fig. 11(a). However, the color-gradient model fails to capture the correct curvature due to its artificial phase separation characteristic, causing a breakthrough without any $|\nabla P|$, as shown in Fig. 11(b).

We compare the behavior of ganglia with identical volume V but different initial pore occupancies n in an external field. Specifically, we examine ganglia A1, A2, and A3, each with a volume $V = 8V_{\text{pore}}$, but with initial pore occupancies of $n = 8$, $n = 10$, and $n = 9$, respectively, as shown in Fig. 12. All ganglia A1, A2, and A3 eventually reach configuration D as *Bo* increases. Ganglion A1 undergoes a breakthrough at its leading edge, while A2 experiences a flinch at its tail. In contrast, A3 does not exhibit any breakthrough or flinch during the process. These findings are consistent with Fig. 3(a) in Ref. 80.

In this section, we discuss the immiscible-flow regime within a homogeneous 2D rock sample whose structural data comes from the Research Institute of Petroleum Exploration & Development (RIPED),[81] as shown in Fig. S10(a). The sample size is $0.15 \times 0.15\,\text{mm}^2$ and the permeability is 600 m/d with porosity 33.26%, which can be calculated using an ordinary single-phase LBM scheme. In the calculations, water and oil densities are $\rho_w = \rho_o = 1000\,\text{kg/m}^3$, kinematic viscosities are $\upsilon_w = \upsilon_o = 1 \times 10^{-6}\,\text{m}^2/\text{s}$, and the surface tension is $\gamma = 0.015\,\text{N/m}$, corresponding to lattice densities $\rho_w = \rho_o = 1$, lattice kinematic viscosities $\upsilon_w = \upsilon_o = 0.1667$, and lattice surface tension $\gamma = 0.1543$. Four capillary numbers are considered: $Ca = 4 \times 10^{-5}$, $Ca = 3 \times 10^{-4}$, $Ca = 2 \times 10^{-3}$ at $M = 1$, and $Ca = 5 \times 10^{-4}$ at different oil/water viscosity ratios under fully water-wet conditions ($\theta_w = 0°$). The capillary number definition matches that in Sec. II. We use $400 \times 400\,\text{lu}^2$ to describe the sample, and body forces in the *x*-direction are applied to each phase to achieve the prescribed *Ca*. The computational domain is symmetrically configured to ensure periodicity, resulting in a domain size of $800 \times 400\,\text{lu}^2$, as shown in Fig. S10(b). For each prescribed water saturation S_w (and, thus, $S_o = 1 - S_w$), the initial two-phase distribution is generated by a random seeding (random-point sprinkling) procedure within the pore space: we randomly assign the minority phase to a corresponding fraction of fluid nodes to match the target saturation, then run a short relaxation without external forcing to remove initialization transients before applying the body forces to measure steady-state mobilities. This randomized initialization minimizes bias from any particular deterministic initial morphology.

To evaluate the fluids flow capacity vs saturation under different *Ca*, we define the relative mobilities of water and oil as

$$m_{r,w} = \frac{\bar{u}_w}{\bar{u}_{D,w}}, \qquad m_{r,o} = \frac{\bar{u}_o}{\bar{u}_{D,o}}, \tag{29}$$

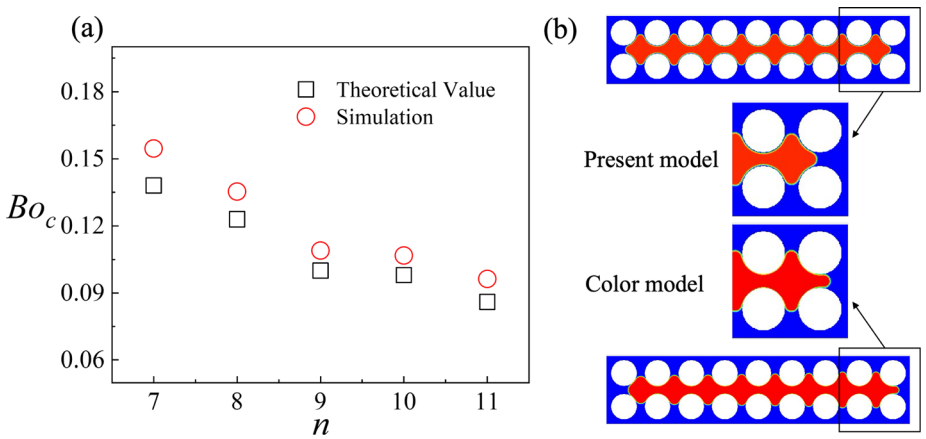

FIG. 11. (a) Comparison between theoretical and simulated critical Bond numbers Bo_c. (b) Initial state for $n = 8$ in the present model and the color-gradient model.

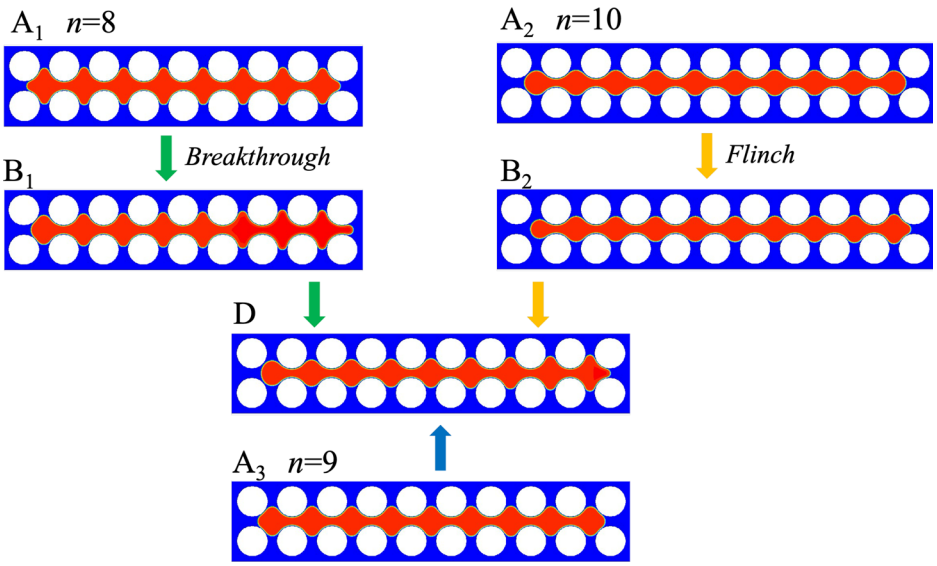

FIG. 12. Evolution of ganglia with identical volume $V = 8V_{pore}$ but different initial pore occupancies (A_1, A_2, and A_3) under increasing *Bo*.

where $\bar{u}_w$ and $\bar{u}_o$ represent the water and oil average velocity at given saturation S_w and S_o under a specific *Ca* and $\bar{u}_{D,w}$ $\bar{u}_{D,o}$ are single-phase average velocity under the same body force as the two-phase flow, which is used to achieve the specified *Ca*.

Accurate velocity data are essential for obtaining relative mobility, yet such data are often interfered by spurious currents. Previous studies have investigated relative mobility using various immiscible multi-phase LB models,[2,40–42,51–54,57,82–88] while their work lacked of analyzing the impact of spurious currents and failed to present velocity contours. Take $\bar{u}_w$ as an example. $\bar{u}_w$ consists of two terms: spurious currents $\bar{u}_s$ and physical velocity $\bar{u}_p$, so the relative mobility can be rewritten as

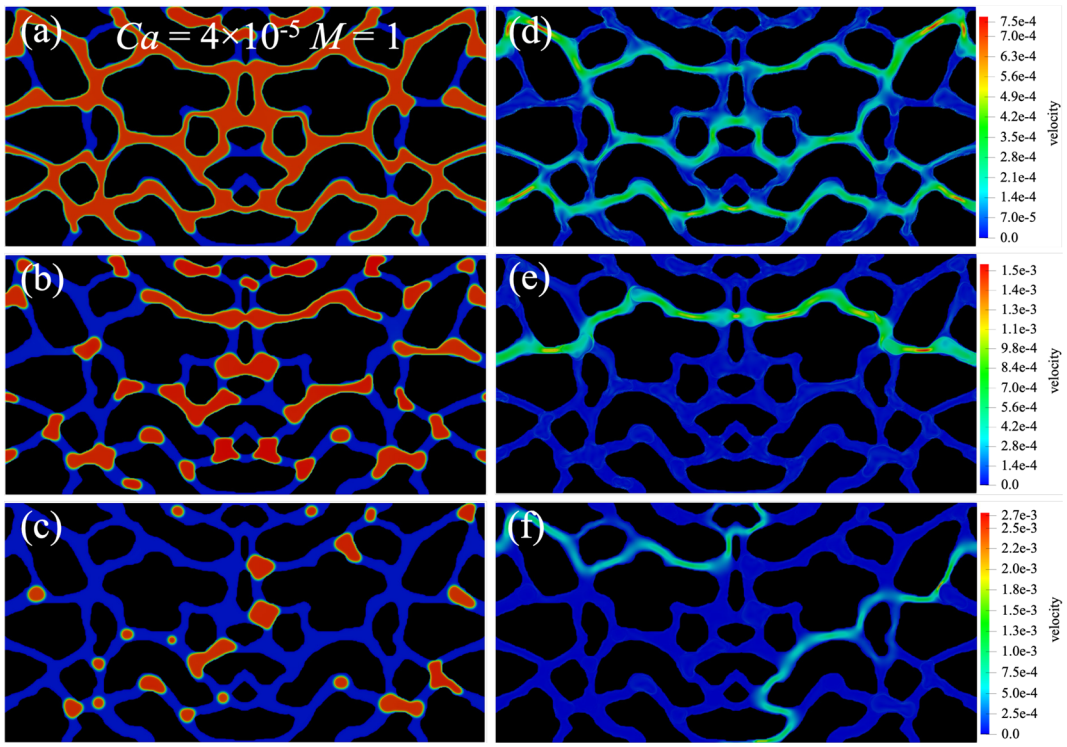

FIG. 13. Phase distributions and velocity contours at $Ca = 4 \times 10^{-5}$ and $M = 1$ for (a)–(c) $S_w = 0.2$, 0.5, and 0.8, respectively, with corresponding velocity contours shown in panels (d)–(f). The initial phase distributions are generated by random seeding at the target saturation and then relaxed before applying the driving forces.

$$m_{r,w} = \frac{\bar{u}_{s,w} + \bar{u}_{p,w}}{\bar{u}_{D,w}}, \qquad m_{r,o} = \frac{\bar{u}_{s,o} + \bar{u}_{p,o}}{\bar{u}_{D,o}}. \tag{30}$$

Capillary number indicates the relative magnitude of viscous force to interfacial tension in immiscible flows. Under identical phase distribution, increasing Ca corresponds to stronger viscous dominance, which enhances relative mobility. However, $\bar{u}_s$ may overwhelm $\bar{u}_p$ when Ca is small, causing the relative mobility to decrease as Ca increases. This violates the physical expectation and renders simulations unreliable. In our simulation, the basic physical criterion is satisfied even at $Ca = 4 \times 10^{-5}$, $M = 1$ and $Ca = 5 \times 10^{-4}$, $M = 100$. The simulated phase distributions and velocity contours are shown in Figs. 13 and 14. Deep blue represents water, red denotes oil, and black indicates solid rock.

The $m_r - S_w$ curves at different Ca and M are shown in Fig. 15(a). Water remains immobile until its saturation reaches $S_w = 0.4$, whereas oil begins to flow at $S_o = 0.3$ when $Ca = 4 \times 10^{-5}$ and $S_o = 0.2$ when $Ca \geq 3 \times 10^{-4}$. The maximum $m_{r,w}$ is only 0.1 at $Ca = 4 \times 10^{-5}$, owing to the "Jamin" effect. Even when oil becomes the continuous phase [Fig. 14(a)], the maximum $m_{r,o}$ is just 0.5

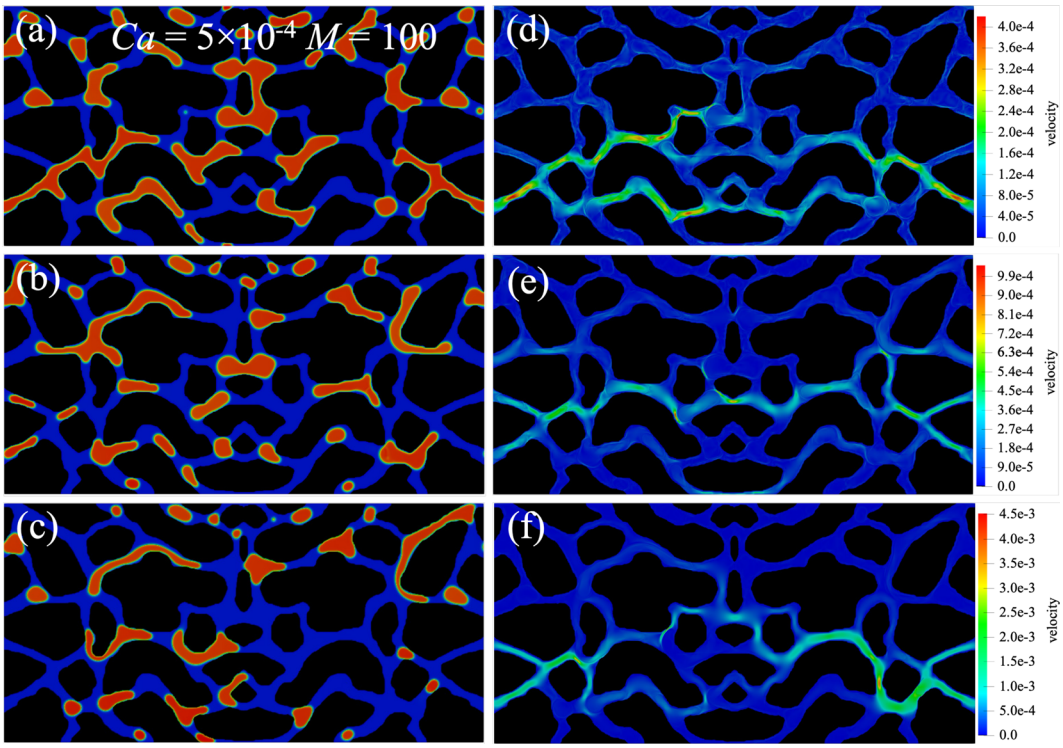

FIG. 14. Phase distributions and velocity contours at $Ca = 5 \times 10^{-4}$ and $M = 100$ for (a)–(c) $S_w = 0.5$, 0.6, and 0.7, respectively, with corresponding velocity contours shown in panels (d)–(f). The initial phase distributions are generated by random seeding at the target saturation and then relaxed before applying the driving forces.

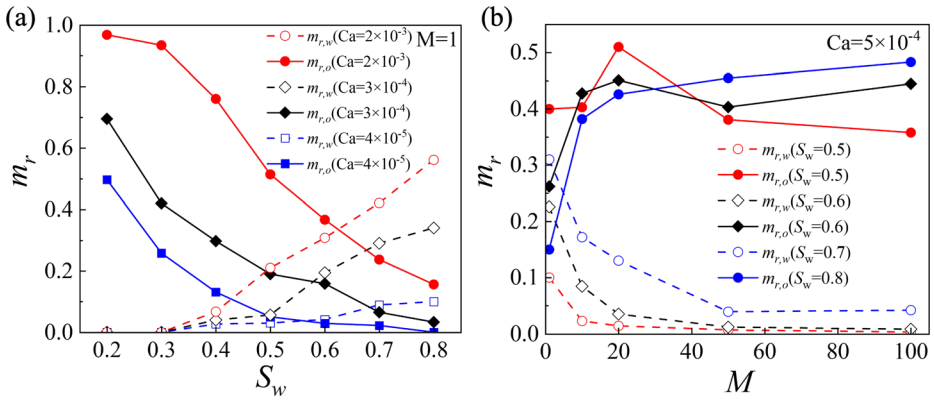

FIG. 15. (a) Relative mobility curves under different Ca at $M = 1$. (b) Variation of relative mobility with viscosity ratio M at fixed saturation for $Ca = 5 \times 10^{-4}$.

because static water films act as solid walls, producing substantial resistance. As Ca increases, both $m_{r,w}$ and $m_{r,o}$ rise due to stronger viscous forces. In general, $m_{r,w}$ remains smaller than $m_{r,o}$ under equivalent saturation because the wetting phase prefers to flow along the solid interface. Figure 14(b) demonstrates that $m_{r,w}$ decreases with increasing M, reaching 0.003 at $S_w = 0.5$ and 0.042 at $S_w = 0.7$ due to viscous coupling. Furthermore, $m_{r,o}$ depends on M and $m_{r,w}$:[60] larger M and $m_{r,w}$ enhance the viscous coupling effect. However, the two factors act in opposite directions on relative mobility, leading to an extremum for $m_{r,w}$.

All simulations in this work employ periodic boundary conditions, which are well suited for the present benchmarks because they represent fully developed bulk flow and avoid inlet/outlet artifacts that can obscure the measurement of steady spurious currents and relative mobilities. For displacement problems with imposed velocity/pressure boundary conditions (inflow/outflow), periodicity is not directly applicable, and one must use appropriate open-boundary schemes (e.g., pressure or velocity boundaries) for the distribution functions and phase fields. A practical implementation detail for the proposed E10 interaction force is that its extended stencil requires additional layers of ghost nodes near the inlet/outlet to evaluate the high-order force consistently; in our D2Q37-based E10 stencil, this corresponds to adding several (typically three) ghost layers and filling them using the chosen boundary extrapolation.

IV. CONCLUSION AND DISCUSSION

This work provides a physically grounded and implementation-ready strategy to suppress spurious currents in multicomponent pseudopotential lattice Boltzmann simulations of immiscible flow, with particular focus on disordered/porous media and high viscosity ratios.

From a modeling perspective, the dominant errors in the conventional multicomponent pseudopotential model originate from the discrete approximation of the intercomponent interaction force: finite-order stencils break rotational isotropy and do not preserve an exact discrete force balance across a curved interface. The resulting interaction-force residual contains non-hydrostatic components, which can be decomposed into solenoidal and irrotational parts; even in nominally static configurations, the solenoidal component acts as an effective spurious driving and generates parasitic vortical motion. Because this error is primarily a stencil-anisotropy effect (rather than a pure resolution error), grid refinement reduces the spurious capillary number only weakly. These observations motivate our two-pronged strategy: improve force isotropy (E10) to strongly suppress the solenoidal residual and then use longitudinal-viscosity control to damp the remaining irrotational response.

The main pointwise conclusions are

1. **Helmholtz–Hodge mechanism and viscosity pathways.** By applying a Helmholtz–Hodge decomposition to the discrete interaction-force residual, we show that spurious-current driving errors can be separated into solenoidal (vortical) and irrotational (compressive) channels. These two channels couple to hydrodynamics through distinct viscosity pathways: the solenoidal component is damped by the shear viscosity μ (controlled by s_ν), whereas the irrotational component is damped by the longitudinal viscosity $\lambda = \zeta + \frac{4}{3}\mu$ (controlled by s_e and s_ϵ). This mapping clarifies when and why MRT relaxation parameters attenuate spurious currents, turning mitigation from empirical tuning into a physics-guided procedure linked to non-conserved moments.
2. **High-order isotropy as a channel selector.** A tenth-order isotropic (E10) interaction-force construction shifts the residual error overwhelmingly into the irrotational channel. As a result, increasing λ via tuning s_e and s_ϵ becomes a principled lever to suppress parasitic motion without compromising surface-tension fidelity.
3. **Quantified reduction of the solenoidal residual and spurious currents.** Fourier-space analyses and simulation-based decompositions demonstrate that the E10 stencil reduces the solenoidal share of the residual by three to four orders of magnitude relative to the conventional E4 stencil, thereby activating bulk-/longitudinal-viscosity control as the dominant suppression mechanism. This delivers about two orders of magnitude reduction in spurious currents and enables stable simulations at large viscosity ratios relevant to complex disordered media.
4. **Robust performance across benchmarks and porous-media applications.** Across static and dynamic tests (Laplace pressure and two-component Poiseuille flow), the method consistently reduces the spurious capillary number to $Ca_s \sim 10^{-5}$ and remains stable up to viscosity ratios of $M \approx 200$. In stringent interfacial-flow problems—including Taylor–Bretherton bubble dynamics down to $Ca = 0.002$, the startup of trapped ganglia in porous media, and immiscible flow in digitized rocks under extreme wettability—the model reproduces theoretical predictions and physical scaling laws that are often masked by spurious currents in traditional approaches.

This framework can be extended to three-dimensional simulations with D3Q19/D3Q27 stencils, higher density ratios, and more complex equations of state; coupled with GPU-based high-performance computing, it will enable predictive pore-scale modeling in applications including enhanced oil recovery (EOR), CO_2 sequestration, and fuel-cell water–gas management.

SUPPLEMENTARY MATERIAL

See the supplementary material for additional details on parameter consistency, including the influence of intercomponent interaction strength, viscosity, and fluid–solid coupling on surface tension, interface thickness, and spurious currents. Specifically, Fig. S1 quantifies the effect of $g_{\sigma\sigma'}$ on surface tension, interface thickness, and spurious currents; Fig. S2 summarizes how viscosity affects spurious currents and the corresponding spurious Reynolds and capillary numbers; and Fig. S3 verifies the contact angles produced by the fluid–solid interaction model. It also includes Laplace-law verification (Fig. S4), a porous-media grid-resolution study (Fig. S5), viscosity distribution and spurious-current fields in porous media (Figs. S6 and S7), and supporting geometries and simulation setups for Taylor/Bretherton flow, trapped-ganglia startup, and digitized-rock simulations (Figs. S8–S10).

ACKNOWLEDGMENTS

We gratefully acknowledge the financial support and funding provided by the National Natural Science Foundation of China under Grant No. 12172010, the National Key Research and Development Program of China under Grant No. 2023YFA1011700, and the China National Petroleum Corporation–Peking University Strategic Cooperation Project of Fundamental Research. We declare no conflict of interest.

AUTHOR DECLARATIONS

Conflict of Interest

The authors have no conflicts to disclose.

Author Contributions

Jingsen Feng: Conceptualization (equal); Data curation (equal); Formal analysis (equal); Investigation (equal); Methodology (equal); Software (equal); Validation (equal); Visualization (equal); Writing – original draft (equal). **Chuanxi Wang:** Validation (equal). **Yingyang Guo:** Writing – review & editing (equal). **Yang Liu:** Conceptualization (equal). **Jingchun Min:** Funding acquisition (equal). **Moran Wang:** Conceptualization (equal). **Ke Xu:** Funding acquisition (equal); Writing – review & editing (equal).

DATA AVAILABILITY

The data that support the findings of this study are available within the article and its supplementary material.

REFERENCES

[1]F. Liu and M. Wang, "Trapping patterns during capillary displacements in disordered media," J. Fluid Mech. **933**, A52 (2022).
[2]N. Suwandi, F. Jiang, and T. Tsuji, "Relative permeability variation depending on viscosity ratio and capillary number," Water Resour. Res. **58**, e2021WR031501, https://doi.org/10.1029/2021WR031501 (2022).
[3]P. K. Yadav and P. Srivastava, "Impact of porous material and slip condition on the MHD flow of immiscible couple stress-Newtonian fluids through an inclined channel: Head loss and pressure difference," Chin. J. Phys. **89**, 1198 (2024).
[4]P. K. Yadav and A. Verma, "Analysis of the MHD flow of immiscible fluids with variable viscosity in an inclined channel," J. Appl. Mech. Tech. Phys. **64**, 618 (2023).
[5]S. Leclaire, A. Parmigiani, O. Malaspinas, B. Chopard, and J. Latt, "Generalized three-dimensional lattice Boltzmann color-gradient method for immiscible two-phase pore-scale imbibition and drainage in porous media," Phys. Rev. E **95**, 033306 (2017).
[6]T. Reis, "A lattice Boltzmann formulation of the one-fluid model for multiphase flow," J. Comput. Phys. **453**, 110962 (2022).
[7]A. Sedahmed, R. R. Coelho, N. A. M. Araújo, M. A. Wahba, and H. A. Warda, "Study of fluid displacement in three-dimensional porous media with an improved multi-component pseudopotential lattice Boltzmann method," Phys. Fluids **34**, 103303 (2022).
[8]L. Fei, F. Qin, J. Zhao, D. Derome, and J. Carmeliet, "Lattice Boltzmann modelling of isothermal two-component evaporation in porous media," J. Fluid Mech. **955**, A18 (2023).
[9]C.-S. Li, R.-R. Cai, and L. Zhang, "An improved immersed moving boundary-based curved wetting condition method for the pseudopotential multiphase lattice Boltzmann model," Phys. Fluids **36**, 112119 (2024).
[10]X. Shan, "Analysis and reduction of the spurious current in a class of multiphase lattice Boltzmann models," Phys. Rev. E **73**, 047701 (2006).
[11]K. Connington and T. Lee, "A review of spurious currents in the lattice Boltzmann method for multiphase flows," J. Mech. Sci. Technol. **26**, 3857 (2012).
[12]Z. Qin, W. Chen, C. Qin, X. Xu, and B. Wen, "Spurious currents suppression by accurate difference schemes in multiphase lattice Boltzmann method," Comput. Fluids **261**, 105917 (2023).
[13]T. Lafarge, P. Boivin, N. Odier, and B. Cuenot, "Improved color-gradient method for lattice Boltzmann modeling of two-phase flows," Phys. Fluids **33**, 082110 (2021).
[14]S. Saito, N. Takada, S. Baba, S. Someya, and H. Ito, "Generalized equilibria for color-gradient lattice Boltzmann model based on higher-order Hermite polynomials: A simplified implementation with central moments," Phys. Rev. E **108**, 065305 (2023).
[15]S. Zhang, H. Wu, S. Lin, G. Jiang, and Z. Liu, "Three-dimensional central-moment pseudopotential lattice Boltzmann model with improved discrete additional term," Phys. Fluids **36**, 103304 (2024).
[16]Z. Guo, "Well-balanced lattice Boltzmann model for two-phase systems," Phys. Fluids **33**, 031709 (2021).
[17]L. Zheng, S. Zheng, and Q. Zhai, "Eliminating spurious currents in phase-field-theory-based lattice Boltzmann equation for two-phase flows," Phys. Fluids **33**, 092102 (2021).
[18]Q. Zhang, M. Jiang, C. Zhuo, C. Zhong, and S. Liu, "Theoretical and numerical study on the well-balanced regularized lattice Boltzmann model for two-phase flow," Phys. Rev. E **108**, 055309 (2023).
[19]H. Bhatia, G. Norgard, V. Pascucci, and P. T. Bremer, "The Helmholtz–Hodge decomposition—A survey," IEEE Trans. Visualization Comput. Graph. **19**, 1386 (2013).
[20]Y. Tong, S. Lombeyda, A. Hirani, and M. Desbrun, "Discrete multiscale vector field decomposition," ACM Trans. Graph. **22**, 445 (2003).
[21]P. Angot, J.-P. Caltagirone, and P. Fabrie, "Fast discrete Helmholtz–Hodge decompositions in bounded domains," Appl. Math. Lett. **26**, 445 (2013).
[22]C. M. O'Reilly and S. T. Grilli, "A lattice-Boltzmann-based perturbation method," Comput. Fluids **213**, 104723 (2020).
[23]C. O'Reilly, S. Grilli, C. Janßen, J. Dahl, and J. Harris, "Hybrid lattice-Boltzmann-potential flow simulations of turbulent flow around submerged structures," J. Mar. Sci. Eng. **10**, 1651 (2022).
[24]S. Schoder, K. Roppert, and M. Kaltenbacher, "Helmholtz's decomposition for compressible flows and its application to computational aeroacoustics," SN Partial Differ. Equations Appl. **1**, 46 (2020).
[25]S. Schoder, "Helmholtz's decomposition for aeroacoustics using a standard flow solver," arXiv:2207.08144 (2022).
[26]Y. Qi, L. Wang, Z. Guo, and S. Chen, "Analysis and removal of spurious pressure oscillations in Boltzmann-equation-based mesoscopic simulation of incompressible turbulence," J. Fluid Mech. **1005**, A9 (2025).
[27]P. J. Dellar, "Hyperbolic divergence cleaning in lattice Boltzmann magnetohydrodynamics," Commun. Comput. Phys. **33**, 245 (2023).
[28]D. d'Humières, "Multiple-relaxation-time lattice Boltzmann models in three dimensions," Philos. Trans. R. Soc., A **360**, 437 (2002).
[29]P. Lallemand and L. Luo, "Theory of the lattice Boltzmann method: Dispersion, dissipation, isotropy, Galilean invariance, and stability," Phys. Rev. E **61**, 6546 (2000).
[30]H. Liu, Q. Kang, C. Leonardi, S. Schmieschek, A. Narváez, B. Jones, J. Williams, A. Valocchi, and J. Harting, "Multiphase lattice Boltzmann simulations for porous media applications," Comput. Geosci. **20**, 777 (2016).
[31]Z. Guo, C. Zheng, and B. Shi, "Discrete lattice effects on the forcing term in the lattice Boltzmann method," Phys. Rev. E **65**, 046308 (2002).
[32]Q. Li, K. Luo, and X. Li, "Forcing scheme in pseudopotential lattice Boltzmann model for multiphase flows," Phys. Rev. E **86**, 016709 (2012).
[33]M. Porter, E. Coon, Q. Kang, J. Moulton, and J. Carey, "Multicomponent interparticle-potential lattice Boltzmann model for fluids with large viscosity ratios," Phys. Rev. E **86**, 036701 (2012).
[34]P. Dellar, "Bulk and shear viscosities in lattice Boltzmann equations," Phys. Rev. E **64**, 031203 (2001).
[35]H. Huang, M. Sukop, and X. Lu, "Multiphase lattice Boltzmann methods: Theory and application," Phys. Rev. E **84**, 046710 (2011).
[36]R. C. Coelho, C. B. Moura, M. M. Telo da Gama, and N. A. Araújo, "Wetting boundary conditions for multicomponent pseudopotential lattice Boltzmann," Int. J. Numer. Methods Fluids **93**, 2570 (2021).
[37]M. Sbragaglia, R. Benzi, L. Biferale, S. Succi, K. Sugiyama, and F. Toschi, "Generalized lattice Boltzmann method with multirange pseudopotential," Phys. Rev. E **75**, 026702 (2007).
[38]C. From, E. Sauret, S. Galindo-Torres, and Y. Gu, "Interaction pressure tensor on high-order lattice Boltzmann models for nonideal fluids," Phys. Rev. E **99**, 063318 (2019).
[39]M. Lulli, L. Biferale, G. Falcucci, M. Sbragaglia, and X. Shan, "Structure and isotropy of lattice pressure tensors for multirange potentials," Phys. Rev. E **103**, 063309 (2021).
[40]A. Ghassemi and A. Pak, "Numerical study of factors influencing relative permeabilities of two immiscible fluids flowing through porous media using lattice Boltzmann method," J. Pet. Sci. Eng. **77**, 135 (2011).
[41]Z. Dou and Z. Zhou, "Numerical study of non-uniqueness of the factors influencing relative permeability in heterogeneous porous media by lattice Boltzmann method," Int. J. Heat Fluid Flow **42**, 23 (2013).

[42]C. Gao, R. Xu, and P. Jiang, "Pore-scale numerical investigations of fluid flow in porous media using lattice Boltzmann method," Int. J. Numer. Methods Heat Fluid Flow **25**, 1957 (2015).
[43]H. Huang, J. Huang, and X. Lu, "Study of immiscible displacements in porous media using a color-gradient-based multiphase lattice Boltzmann method," Comput. Fluids **93**, 164 (2014).
[44]Y. Ba, H. Liu, Q. Li, Q. Kang, and J. Sun, "Multiple-relaxation-time color-gradient lattice Boltzmann model for simulating two-phase flows with high density ratio," Phys. Rev. E **94**, 023310 (2016).
[45]S. Ammar, G. Pernaudat, and J. Trépanier, "A multiphase three-dimensional multi-relaxation time (MRT) lattice Boltzmann model with surface tension adjustment," J. Comput. Phys. **343**, 73 (2017).
[46]D. Wang, F. Liu, J. Sun, Y. Li, Q. Wang, Y. Jiao, K. Song, S. Wang, and R. Ma, "Lattice-Boltzmann simulation of two-phase flow in carbonate porous media retrieved from computed microtomography," Chem. Eng. Sci. **270**, 118514 (2023).
[47]X. Zhu, S. Wang, Q. Feng, L. Zhang, L. Chen, and W. Tao, "Pore-scale numerical prediction of three-phase relative permeability in porous media using the lattice Boltzmann method," Int. Commun. Heat Mass Transfer **126**, 105403 (2021).
[48]H. Liu, S. Sun, R. Wu, B. Wei, and J. Hou, "Pore-scale modeling of spontaneous imbibition in porous media using the lattice Boltzmann method," Water Resour. Res. **57**, e2020WR029219, https://doi.org/10.1029/2020WR029219 (2021).
[49]P. Mora, G. Morra, D. A. Yuen, S. Patil, and R. Juanes, "Convection–diffusion with the colour gradient lattice Boltzmann method for three-component, two-phase flow," Transp. Porous Media **147**, 259 (2023).
[50]Q. Gu, H. Liu, and L. Wu, "Preferential imbibition in a dual-permeability pore network," J. Fluid Mech. **915**, A138 (2021).
[51]A. Yiotis, J. Psihogios, M. Kainourgiakis, A. Papaioannou, and A. Stubos, "A lattice Boltzmann study of viscous coupling effects in immiscible two-phase flow in porous media," Colloids Surf., A **300**, 35 (2007).
[52]H. Huang and X. Lu, "Relative permeabilities and coupling effects in steady-state gas-liquid flow in porous media: A lattice Boltzmann study," Phys. Fluids **21**, 092104 (2009).
[53]H. Huang, Z. Li, S. Liu, and X. Lu, "Shan-and-chen-type multiphase lattice Boltzmann study of viscous coupling effects for two-phase flow in porous media," Int. J. Numer. Methods Fluids **61**, 341 (2009).
[54]T. Ramstad, P.-E. Øren, and S. Bakke, "Simulation of two-phase flow in reservoir rocks using a lattice Boltzmann method," SPE J. **15**, 917 (2010).
[55]F. Gharibi and M. Ashrafizaadeh, "Simulation of high-viscosity-ratio multicomponent fluid flow using a pseudopotential model based on the nonorthogonal central-moments lattice Boltzmann method," Phys. Rev. E **101**, 043311 (2020).
[56]H. Otomo, B. Crouse, M. Dressler, D. Freed, I. Staroselsky, R. Zhang, and H. Chen, "Multi-component lattice Boltzmann models for accurate simulation of flows with wide viscosity variation," Comput. Fluids **172**, 674 (2018).
[57]H. Zhao, Z. Ning, Q. Kang, L. Chen, and T. Zhao, "Relative permeability of two immiscible fluids flowing through porous media determined by lattice Boltzmann method," Int. Commun. Heat Mass Transfer **85**, 53 (2017).
[58]X. Shan and H. Chen, "Lattice Boltzmann model for simulating flows with multiple phases and components," Phys. Rev. E **47**, 1815 (1993).
[59]X. Shan and H. Chen, "Simulation of nonideal gases and liquid-gas phase transitions by the lattice Boltzmann equation," Phys. Rev. E **49**, 2941 (1994).
[60]J. Feng, Y. Liu, and J. Min, "A pore-scale investigation of viscous coupling effect on immiscible two-phase flow in porous media," Chem. Eng. Res. Des. **211**, 379 (2024).
[61]S. Leclaire, M. Reggio, and J. Y. Trépanier, "Isotropic color gradient for simulating very high-density ratios with a two-phase flow lattice Boltzmann model," Comput. Fluids **48**, 98 (2011).
[62]S. Leclaire, N. Pellerin, M. Reggio, and J. Y. Trépanier, "Enhanced equilibrium distribution functions for simulating immiscible multiphase flows with variable density ratios in a class of lattice Boltzmann models," Int. J. Multiphase Flow **57**, 159 (2013).
[63]S. Leclaire, N. Pellerin, M. Reggio, and J. Trépanier, "An approach to control the spurious currents in a multiphase lattice Boltzmann method and to improve the implementation of initial condition," Int. J. Numer. Methods Fluids **77**, 732 (2015).
[64]P. Aussillous and D. Quéré, "Quick deposition of a fluid on the wall of a tube," Phys. Fluids **12**, 2367 (2000).
[65]G. Taylor, "Deposition of a viscous fluid on the wall of a tube," J. Fluid Mech. **10**, 161 (1961).
[66]F. P. Bretherton, "The motion of long bubbles in tubes," J. Fluid Mech. **10**, 166 (1961).
[67]A. Kuzmin, M. Januszewski, D. Eskin, F. Mostowfi, and J. Derksen, "Simulations of gravity-driven flow of binary liquids in microchannels," Chem. Eng. J. **171**, 646 (2011).
[68]M. D. Giavedoni and F. A. Saita, "The axisymmetric and plane cases of a gas phase steadily displacing a Newtonian liquid—A simultaneous solution of the governing equations," Phys. Fluids **9**, 2420 (1997).
[69]M. Heil, "Finite Reynolds number effects in the Bretherton problem," Phys. Fluids **13**, 2517 (2001).
[70]H. E. Huppert and J. A. Neufeld, "The fluid mechanics of carbon dioxide sequestration," Annu. Rev. Fluid Mech. **46**, 255 (2014).
[71]Y. Sun, Q. Li, D. Yang, and X. Liu, "Laboratory core flooding experimental systems for CO_2 geosequestration: An updated review over the past decade," J. Rock Mech. Geotech. Eng. **8**, 113 (2016).
[72]M. Tuller and D. Or, "Hydraulic conductivity of variably saturated porous media: Film and corner flow in angular pore space," Water Resour. Res. **37**, 1257, https://doi.org/10.1029/2000WR900328 (2001).
[73]R. Haggerty, D. Zhang, J. Eun, and Y. Li, "Characterization of bubble transport in porous media using a microfluidic channel," Water **15**, 1033 (2023).
[74]E. Shahraeeni and D. Or, "Pore scale mechanisms for enhanced vapor transport through partially saturated porous media," Water Resour. Res. **48**, W05502, https://doi.org/10.1029/2011WR011036 (2012).
[75]L. Chen, M. Wang, Q. Kang, and W. Tao, "Pore scale study of multiphase multicomponent reactive transport during CO2 dissolution trapping," Adv. Water Resour. **116**, 208 (2018).
[76]R. Larson, L. Scriven, and H. Davis, "Percolation theory of residual phases in porous media," Nature **268**, 409 (1977).
[77]R. Larson, L. Scriven, and H. Davis, "Percolation theory of two phase flow in porous media," Chem. Eng. Sci. **36**, 57 (1981).
[78]S. Datta, T. Ramakrishnan, and D. Weitz, "Mobilization of a trapped non-wetting fluid from a three-dimensional porous medium," Phys. Fluids **26**, 022002 (2014).
[79]M. Yeganeh, J. Hegner, E. Lewandowski, A. Mohan, L. Lake, D. Cherney, A. Jusufi, and A. Jaishankar, "Capillary desaturation curve fundamentals," in *SPE Improved Oil Recovery Conference* (SPE, 2016).
[80]C. Wang and K. Xu, "Ganglion startup in porous media," Chem. Eng. Sci. **292**, 119982 (2024).
[81]C. Xie, W. Lv, and M. Wang, "Shear-thinning or shear-thickening fluid for better EOR?—A direct pore-scale study," J. Pet. Sci. Eng. **161**, 683 (2018).
[82]D. Zhang, K. Papadakis, and S. Gu, "A lattice Boltzmann study on the impact of the geometrical properties of porous media on the steady state relative permeabilities on two-phase immiscible flows," Adv. Water Resour. **95**, 61 (2016).
[83]W. Chen and F. Jiang, "Impact of PTFE content and distribution on liquid-gas flow in PEMFC carbon paper gas distribution layer: 3D lattice Boltzmann simulations," Int. J. Hydrogen Energy **41**, 8550 (2016).
[84]S. Li, F. Jiang, B. Wei, J. Hou, and H. Liu, "Prediction of three-phase relative permeabilities of Berea sandstone using lattice Boltzmann method," Phys. Fluids **33**, 063302 (2021).
[85]T. Zhang, F. Javadpour, J. Li, Y. Zhao, L. Zhang, and X. Li, "Pore-scale perspective of gas/water two-phase flow in shale," SPE J. **26**, 828 (2021).
[86]Y. Ji, T. Kneafsey, J. Hou, J. Zhao, C. Liu, and T. Guo, "Relative permeability of gas and water flow in hydrate-bearing porous media: A microscale study by lattice Boltzmann simulation," Fuel **321**, 124013 (2022).
[87]D. Zhang, Y. Li, N. Mei, H. Yuan, and C. Shu, "Pore-scale investigation on the effect of icing on relative permeability of two-phase immiscible fluids," Phys. Fluids **35**, 023329 (2023).
[88]Y. Shi and G. Tang, "Relative permeability of two-phase flow in three-dimensional porous media using the lattice Boltzmann method," Int. J. Heat Fluid Flow **73**, 101 (2018).